The Nansen Environmental and Remote Sensing Center

a non-profit
research institute affiliated with
the University of Bergen

Thormøhlensgate 47,
N-5006 Bergen
Norway

NERSC Technical Report no. 366

GCRIEBER
Climate Research Institute

CLIMATOLOGY OF THE HIGH LATITUDES

EXTENDED PROCEEDINGS

OF THE JOINT GC RIEBER CLIMATE INSTITUTE (GCR) AND
PAN-EURASIAN EXPERIMENT (PEEX)
WORKSHOP AT NERSC 29 SEPTEMBER 2015

Editors

Igor Esau and Lasse Pettersson

Bergen, February 29, 2016

Nansen Environmental and Remote Sensing Center

Thormøhlens gate 47
N-5006 Bergen - NORWAY
Phone: +47 55 20 58 00 Fax. +47 55 20 58 01
E-mail: administrasjon@nersc.no Web.site: http://www.nersc.no

a non-profit environmental research center affiliated with the university of Bergen

REPORT

TITLE **Climatology of the high latitudes**	**REPORT No.** Technical report no. 366 **DOI:** 10.13140/RG.2.1.1568.7442
CLIENT Pan-Eurasian Experiment and NordForsk Top-Level Research Initiative CRAICC-PEEX	**CONTRACT** NordForsk TFI No. 26060
CONTACT PERSONS Jostein Sundet (NordForsk)	**AVAILABILITY** OPEN
EDITORS Igor Esau and Lasse Pettersson	**DATE** February 29, 2016

SUMMARY

The Climate Processes Group – GC Rieber Climate Institute (GCR) at the Nansen Environmental and Remote Sensing Centre is developing a coherent research strategy to address the scientific challenges of the rapidly warming high latitudes of the Earth. This workshop summarized the available expertise in the GCR and drafted ideas for perspective research directions compatible with the international Pan-Eurasian Experiment (PEEX) (Lappalainen et al., 2015). PEEX (https://www.atm.helsinki.fi/peex/) is a multidisciplinary, multi-scale bottom-up open scientific initiative. The PEEX approach emphasizes that solving challenges related to climate change, air quality and cryospheric change requires large-scale coordinated co-operation of the international research communities. A scientific workshop was hosted at the Nansen Center (GCR) on 29 the September 2015. The workshop presentations discussed both the large- and small-scale components of the climatology of the high-latitudes. A particular attention has been given to the links between climate scales as well as to the scales shaping the climate impact on society.

Key words: High-latitude climate: Linking large and small scales; climate modeling

APPROVAL *Igor Esau*	*Johnny Johannessen, Director*

Table of Contents

List of Contributors

NERSC & GCR	External
Igor Esau*	Ingo Bethke (Uni Research, Bergen)
Stephen Outten*	Mikhail Varentsov (Lomonosov Moscow State University, Faculty of Geography, Dept. of Meteorology and Climatology, Moscow)
Richard Davy*	Andrey Gritsun* (Institute for Numerical Mathematics, Russian Academy of Science)
Linling Chen*	Joachim Reuder (University in Bergen, Bergen)
Victoria Miles*	Peter Thorne (Maynooth University, Ireland)
Tobias Wolf*	Odd Helge Otterå (Uni Research, Bergen)
Anna Mikalsen	Alexander Chernokulsky (A. M. Obukhov Institute for Atmospheric Physics, Moscow)
Lisbeth Iversen	Martin Miles (Uni Research, Bergen)
Ola M. Johannessen (also Nansen Society, Bergen)	

* Giving oral presentations.

Introduction

"Climate Processes" is the focus research area of the GC Rieber Climate Research Institute at NERSC. This is, however, a challenging area as the processes are very diverse and operate on a multitude of scales. Moreover, the processes actively interact with the large-scale atmospheric and ocean dynamics. The difficulties in creating a coherent approach to study climate processes motivated us to prepare a special group workshop. Considerable effort has been spent developing stronger collaboration within the group while at the same time realizing the existing synergies of our coherent research within and external to NERSC. We believe that this short summary of our combined research will prove useful for our colleagues and be beneficial in the organization of the future cross-disciplinary research proposals. This extended proceeding reports on the current – as at the end of 2015 – lines of research within the GCR group. However, it also provides a glimpse of our future work, particularly in terms of methodology and problem formulation.

The first GCR workshop took place on 29th September 2015 and the Nansen Center. This workshop was related to the Nordic Research Council (NordForsk) networking project CREICC-PEEX. It was therefore an optimal venue to present the group's expertise available to the international Pan-Eurasian Experiment (PEEX) community [Lappalainen et al., 2014]. PEEX (https://www.atm.helsinki.fi/peex/) is a multidisciplinary, multi-scale, bottom-up open research initiative. The PEEX approach emphasizes that solving challenges related to climate change, air quality, and cryospheric change requires large-scale coordinated co-operation of the international research communities.

The contributions presented here are broadly separated into studies of the large-scale and the small-scale components of the climatology of the high-latitudes. Some contributions cannot be clearly classified as they address multiscale phenomena. Particular attention is given to the processes that link climate scales and to the scales that shape the climate impact on society. A significant proportion of current climate research cannot be directly transferred to applied problem solutions for society and implementation of mitigation actions. New approaches to limit the "bottleneck" of the climate knowledge transfer to actions are timely needed. This proceeding includes a few contributions with original ideas specifically along these lines. For example, a solicited contribution by A. Gritsun [see also Gritsun and Brandstator, 2007] introduces a new approach to link the cause and response in climate modelling that is based on the most recent developments in the area of fluctuation-dissipation theory.

Finally, we hope that this extended proceeding will serve as a starting point for synchronizing the cross-group research efforts between the Nansen Environmental and Remote Sensing Centre, the Nansen Scientific Society, and more broadly the Bjerknes Centre for Climate Research, with the international PEEX scientific community.

References

Lappalainen H.K., Petäjä, T., Kujansuu, J., Kerminen, V.-M., Shvidenko, A., Bäck, J., Vesala, T., Vihma, T., de Leeuw, G., Lauri, A., Ruuskanen, T., Lapshin, V.B., Zaitseva, N., Glezer, O., Arshinov, M., Spracklen, D.V., Arnold, S.R., Juhola, S., Lihavainen, H., Viisanen, Y., Chubarova, N., Chalov, S., Filatov, N., Skorokhod, A., Elansky, N., Dyukarev, E., Esau, I., Hari, P., Kotlyakov, V., Kasimov, N., Bondur, V., Matvienko, G., Baklanov, A., Mareev, E., Troitskaya, Y., Ding, A., Guo, H, Zilitinkevich, S., Kulmala, M., 2014: Introduction: Pan Eurasian Experiment (PEEX) - A research initiative meeting the grand challenges of the changing environment of hte Northern Paen-Eurasian Arctic-Boreal areas, *Geography, Environment, Sustainability* , 2, 14-48

Gritsun, A. and Brandstator, G. 2007: Climate Response Using a Three-Dimensional Operator Based on the Fluctuation–Dissipation Theorem *J. Atmos. Sci.*, *64*, 2558-2575

Chapter 1. Large-scale climate dynamics

Bjerknes compensation and the multi-decadal variability of heat transports in the Arctic

Stephen Outten, Igor Esau

The meridional transport of heat is a vital component for maintaining the Earth's climate. The atmosphere and ocean transport the energy entering the climate system at the top of the atmosphere in the tropics to the polar regions where it can be radiated into space, allowing the climate system to cool. Understanding the multi-decadal changes of these transports provides an insight into the natural variability of the flow of heat into the Arctic and to the climate system in general. While it is now well established that the global climate change is primarily driven by anthropogenic forcing [Myhre et al. 2013], a good understanding of natural variability is still required in order to determine the proportion of the observed climate change that is attributable to anthropogenic forcing.

Main findings

The theory of Bjerknes Compensation proposes that anomalies of meridional heat transports in the atmosphere and ocean should be approximately equal and opposite.

This study analyses 600 years of the pre-industrial control run simulations with the Bergen climate Model. The analysis revealed a maximum anti-correlation ($r = -0.72$, $p \leq 0.05$) between the anomalies of the atmospheric and ocean meridional heat flux at 67° N. These anomalies show quasi-oscillations at time scales of 60-80 years despite the applied constant climate forcing in the model run.

In 1964, Jacob Bjerknes proposed that the total energy transported by the climate system should remain approximately constant if the ocean heat storage and fluxes at the top-of-the-atmosphere were unchanging [Bjerknes, 1964]. Since heat is transported by the ocean and atmosphere, his idea implies that any large anomalies in the atmospheric heat transport should be balanced by opposing variations in the ocean heat transport, and vice versa; a process that has since been named Bjerknes Compensation (BC). The lack of three dimensional, long term ocean observations makes it impractical to calculate the BC in the real climate system at the present time. However, studies by Shaffrey and Sutton [2006] did manage to identify BC in the pre-industrial control run of the Hadley Centre coupled climate model, HadCM3. They found that the signal was only apparent on decadal time-scales, since on inter-annual and shorter timescales, the variability in the heat storage strongly influenced the upper ocean heat budget, thus reducing the interconnection between the atmosphere and ocean. Their work further showed that the compensation was strongest at high latitudes, peaking around 70N, with much of the variability limited to the Atlantic sector. Further work by Van Der Swaluw et al. [2007] went on to show that the variations in meridional heat transport were associated with changes in the sea surface temperature and sea ice cover in the Greenland and Norwegian Seas.

Bjerknes Compensation was identified in a second global climate model by Jungcluas and Koenigk in 2010. They examined the pre-industrial control run of ECHAM5/MPIOM (European Centre for medium weather forecast–HAMburg/Max-Planck-Institute Ocean Model). They also found that the strongest compensation was found at high latitudes and mainly in the Atlantic sector. They suggested that since the strength of the compensation determines the heat anomalies available to cause strong warming or cooling, the atmosphere and ocean

must act in concert (i.e. not compensating one another) in order to cause dramatic temperature change e.g. the early 20th century warming. While other studies have examined BC and the balance of heat transports in the climate system, they have employed simple energy balance models [Liu et al. 2015] or Intermediate Complexity Climate Models [Farneti and Vallis 2013], thus limiting their applicability to the global climate system; or they have limited their studies to a single region of the globe [Bishop et al. 2015] and identified Bjerknes-like behavior, but as the authors state, this is not true Bjerknes Compensation since it is limited to a local scale balance.

Our work in the GCR Group at NERSC has investigated BC in the Bergen Climate Model, a fully coupled global climate model developed here at NERSC. This model consists of the ARPEGE general atmospheric circulation model from Meteo France coupled to the Miami Isopycnic Coordinate Ocean Model (MICOM). The Bergen Climate Model was used as part of the CMIP3 project, which served as the basis for the IPCC AR4 report. In this study, we have analyzed the meridional heat transports in both the atmosphere and ocean from the pre-industrial control run of the Bergen Climate Model (Figure 1). While the atmosphere shows a distinctive symmetric shape around the equator with peaks of around 4-5 PW occurring at approximately 40N and 40S, the ocean shows a broad peak of around 2.2P at 17N. The atmospheric heath transports are comparable to those found in both HadCM3 and ECHAM5, while the ocean transport is high compared to both of these other models. Trenberth and Caron [2001] estimated the atmosphere and ocean heat transports from the European Centre for Medium-Range Weather Forecast (ECMWF) reanalysis and the National Centers for Environmental Prediction/National Centre for Atmospheric Research (NCEP/NCAR) reanalysis. Again the atmospheric heat transport is similar to those found in both reanalyses, while the ocean heat transport is high compared to the ECMWF reanalysis but lower than that found in the NCEP/NCAR reanalysis. This suggests that the meridional heat transports in the Bergen Climate Model are comparable to those found in other models and reanalyses, with the ocean heat transports in the Northern hemisphere being at the high end of the range.

The theory of Bjerknes Compensation proposes that anomalies of meridional heat transports in the atmosphere and ocean should be approximately equal and opposite. Correlation between the heat transports over the 600-years of the pre-industrial control run revealed a maximum anti-correlation at 67N, similar to the 70N identified in previous studies. The anomalies of heat transports in the atmosphere and ocean at 67N are shown in Figure 2. This shows the strong anti-correlation ($r=-0.72$, $p\leq0.05$) indicating the presence of Bjerknes Compensation. Interestingly, at 67N the atmosphere transports around 2 PW of heat, while the ocean only transports around 0.25 PW. Despite there being almost an order of magnitude difference between the atmospheric and oceanic heat transports at this latitude, the anomalies in the heat transports are approximately the same magnitude (Figure 2). This means the anomalies represent approximately a 1% variation in the atmospheric heat transport but a 10% variation in the ocean heat transport. This lends support to the idea that these anomalies are directly linked to one another. Finally, Figure 2 also highlights the multi-decadal variation in the global heat transports. Since this is from a pre-industrial control run, the forcings applied to the model are constant and yet and variability with a period of around 60-80 years is clearly visible.

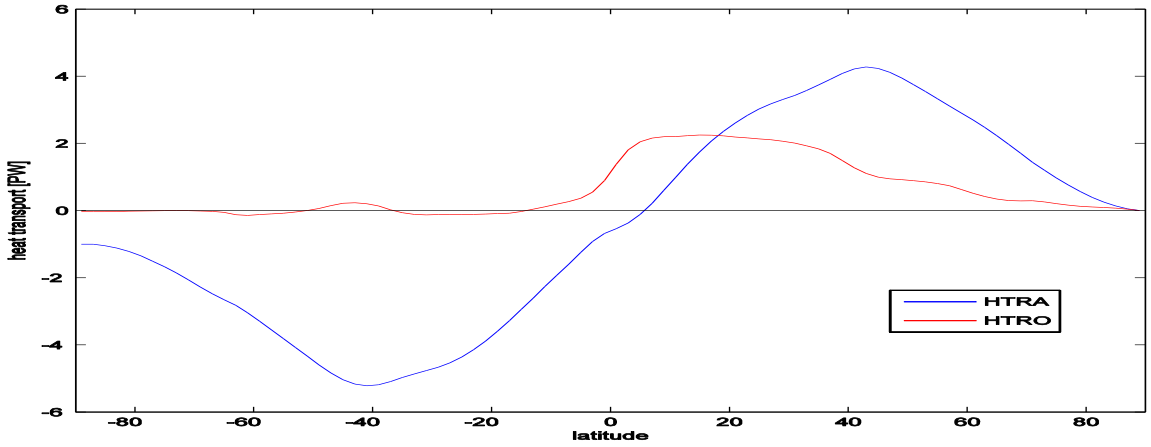

Figure 1: Mean implied meridional heat transports in the atmosphere, (blue), and ocean, (red), in PW as a function of latitude.

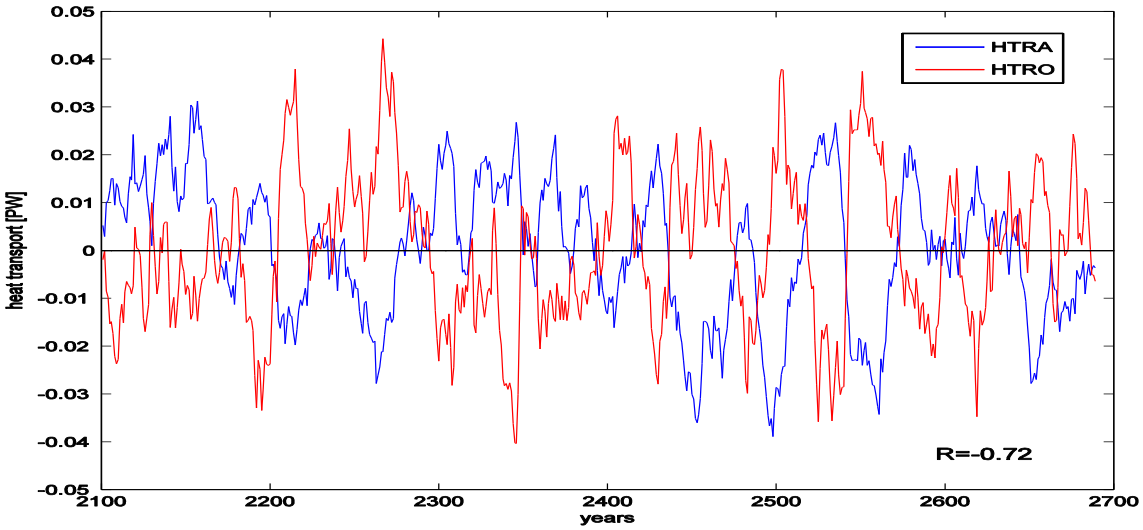

Figure 2: Meridional heat transport anomalies at 67N in the atmosphere (blue) and ocean (red), for the 600 year control run of the Bergen Climate Model. An 11-year running mean has been applied to highlight multi-decadal signals. The anomalies have a correlation of r=-0.72, p≤0.05.

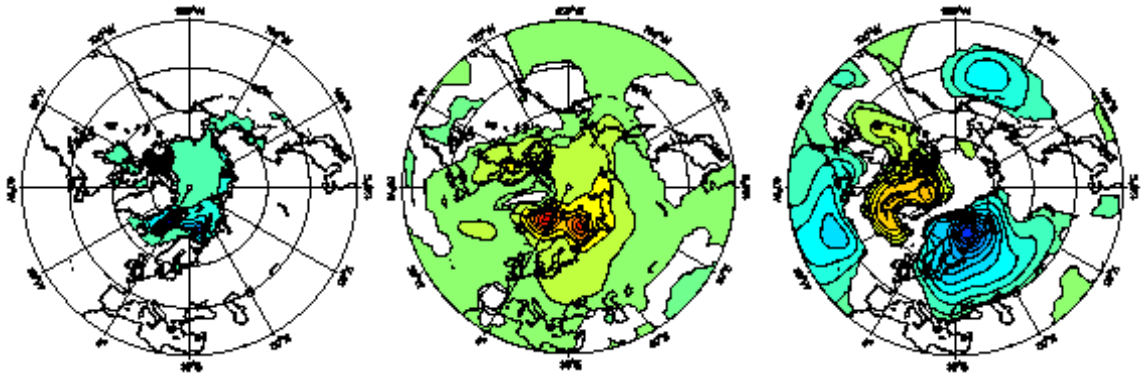

Figure 3: Maps of HTRO regressed onto sea-ice concentration (left), surface air temperature (middle), and sea level pressure (right). Contour levels and units are 2 [%], 0.1 [K], and 2 [Pa] respectively. White regions are below the 95% significance level.

To investigate some of the mechanism behind the natural variability in the heat transports, the ocean heat transport component of the Bjerknes Compensation signal was regressed onto various climate fields in order to determine the spatial patterns associated with this variability. Figure 3 shows that during periods of anomalously high ocean heat transport, sea ice concentration is decreased in the Norwegian and Barents Seas. Where the sea ice is reduced, the warm ocean temperatures are exposed to cold Arctic air, resulting in strong fluxes (not shown) and a sharp rise in the local surface air temperature. This strong but localized heating of the atmosphere causes the formation of thermal low near the surface, as seen in the surface pressure map. In agreement with idealized general circulation simulations performed by Kaspi and Schneider [2011], the localized heating of the atmosphere also gives rise to an upstream stationary high pressure center, in this case located over western Greenland. Further investigations have revealed that the atmospheric response to increase meridional heat transport in the ocean is not limited to the near-surface. Similar regression maps indicate an increase in the 500-hPa geopotential height over the Labrador Sea and Eastern Canada. This suggests that multi-decadal changes to the heat transport in the ocean are associated with changes to the large-scale flow over the North Atlantic. This would not only change the energy available for synoptic systems but may also impact the strength of the ocean gyres, thus feeding back into the ocean.

To investigate this possibility, the changes in strength of the sub-polar gyre over the 600-year pre-industrial control run were compared to the changes in the Bjerknes Compensation signal. A good correlations ($r = 0.52$, $p \leq 0.05$) was found between the strength of the gyre and the atmospheric component of the BC signal, while anomalies of ocean heat transport showed no significant correlation ($r = 0.15$, $p \leq 0.05$), supporting the idea that changes in the atmospheric heat transport are driving changes in the ocean gyre strength.

Our research is ongoing to strengthen this link and complete the understanding of the mechanism that drives the multi-decadal variations in the global heat transports. A new project, SKD-BecomeGyre, has started this year specifically with the aim of investigating links between Bjerknes Compensation the North Atlantic Ocean gyres. At the same time, the research loosely outlined in this section, has been prepared as a journal publication for Climate Dynamics [Outtena and Esau, submitted], and is currently under going revision inline with the reviewers' recommendations. Finally, we are actively participating in and ongoing project, SKD-MEDEVAC, in which we are investigating Bjerknes Compensation in a large number of models from the new CMIP5 archive. The aims of this work are to not only establish the robust existence of the Bjerknes Compensation signal in multiple models, but to determine the impact of this multi-decadal oscillation in the 20th Century simulations, upon which a large amount of current adaptation and mitigation policy is being based.

References

Myhre, G., et al., 2013: Anthropogenic and Natural Radiative Forcing. In: *Climate Change 2013: The Physical Science Basis. Contribution of Working Group I to the Fifth Assessment Report of the Intergovernmental Panel on Climate Change* Cambridge University Press, Cambridge, United Kingdom and New York, NY, USA, pp. 659–740, doi:10.1017/ CBO9781107415324.018.

Bjerknes, J., 1964: Atlantic air-sea interaction. *Adv. in Geophys*., **10**, Academic Press, 1-82

Shaffery, L. C. and R. T. Sutton, 2006: Bjerknes compensation and the decadal variability of energy transports in a coupled climate model. *J. Climate*., **19**, 1167-1181

Van der Swaluw, E., S. S. Drijfhout, and W. Hazeleger, 2007: Bjerknes compensation at high northern latitudes: the ocean forcing the atmosphere. *J. Clim*., **20**, 6023-6032

Jungclaus, J. H. and T. Koenigk, 2010: Low-frequency variability of the arctic climate: the role of oceanic and atmospheric heat transport variations. *Clim. Dyn.*, **34**, 265-279

Liu, Z., H. Yang, C. He and Y. Zhao, (2015) A theory for Bjerknes compensation: the role of climate feedback, *J. Clim.*, Early Online Release

Farneti, R. and G. K. Vallis, (2013) Meridional energy transport in the coupled atmosphere-ocean system: compensation and partitioning, *J. Clim.*, **26**, 7151-7166

Bishop, S. P., F. O. Bryan, and R. J. Small, (2015) Bjerknes-like compensation in the wintertime North Pacific, *J. Phys. Oceanography*, **45**, 1339-1355

Trenberth, K. and J. M. Caron, 2001: Estimates of meridional atmosphere and ocean heat transports, *J. Clim.*, **14**, 3433-3443.

Outten, S. and I. Esau: Bjerknes Compensation in the Bergen Climate Model, *Clim. Dyn.,* in revision

Assessing the role of volcanoes in future climate prediction

Stephen Outten, Ingo Bethke[1], Peter Thorne[2], Odd Helge Otterå[1]

[1] Uni Research, Bergen
[2] Maynooth University, Ireland

Main findings

Plausible, synthetic future volcanic forcings were created based on the magnitude and geographical distribution of volcanic activity in a reconstruction of the past two millennia. Large GCM ensembles were then ran using the Norwegian Earth System model (NorESM) to determine the effect of volcanoes on the projected climate change.

The analysis shows that the potential impact of excluding volcanoes from climate simulations of the future will likely result in an underestimations of both the inter-annual variability and the occurrence of decades with lower and possibly negative global temperature trends.

Volcanoes have been well documented to have both short-term and long-term impacts on the climate system. Explosive volcanic eruptions inject dust, ash and a variety of gases into the atmosphere. The ash and dust has little impact on the climate since it falls out the atmosphere over several days to a few weeks. The major climatic impact of volcanic eruptions comes from the sulfur dioxide released. Sulfur dioxide undergoes chemical reaction in the atmosphere to form sulfate aerosols that increase the reflection of radiation from the sun back into space. This has the effect of cooling the planet. The eruption of Mount Pinatubo in 1991 injected over 20-million tons of sulfur dioxide into the stratosphere, which cooled the Earth's surface for the next three years by as much as 1.3 degrees. While volcanoes also release carbon dioxide, a well known green house gas that acts to warm the atmosphere, they do so in such small quantities compared to anthropogenic emissions that they do not produce a measurable global warming signal.

The radiative effects are however, only the short-term impacts of volcanic eruptions. Volcanic eruptions can also trigger dynamical modifications of the atmospheric circulation that can in turn give rise to large regional climate responses [Stenchikov et al. 2006; Driscoll et al. 2012]. On a more long term basis, eruptions may lead to ocean heat content anomalies and even trigger changes in the ocean circulation [Stenchikov et al. 2009; Otterå et al. 2010; Swingedouw et al. 2015]. Despite this range of impacts on the climate system, volcanic eruptions remain a large source of uncertainty in climate simulations. Future projections of climate, upon which so much mitigation and adaption policy is now being based, exclude volcanoes completely. This issue was raised by the IPPC in its Fifth Assessment Report as follows:

> *"The second effect is that volcanic eruptions are a potential source of uncertainty in our predictions. Eruptions cannot be predicted in advance, but they will occur, causing short-term climatic impacts on both local and global scales. In principle, this potential uncertainty can be accounted for by including random eruptions, or eruptions based on some scenario in our near-term ensemble climate predictions. This area of research needs further exploration. The future projections in this report do not include future volcanic eruptions."*

In this work we have attempted to answer the question to what extent does the exclusion of plausible volcanic activity impact the projections of the 21st Century climate. To this end, we have introduced a novel approach for considering volcanic forcing uncertainty in future

climate assessments. We began by assessing volcanic behavior over the past two millennia. This past volcanic activity was reconstructed based on ice cores taken from Greenland and Antarctica [Sigl et al. 2013]. The depositions from volcanic eruptions that occur in the mid- to high-latitudes are restricted to the hemisphere in which they occur. Therefore, by using ice cores from both hemispheres, Sigl et al. were able to determine which eruptions were tropical and thus appeared in both ice cores, and which were extra-tropical and appeared only in one. Using this reconstruction, we separated the eruptions into three broad locations: tropical, northern hemisphere, southern hemisphere; and three magnitude bands based on peak aerosol optical depth. Figure 1 shows the frequency of volcanic eruptions in each of these categories from the two millennia reconstruction. For each of these nine categories, we were then able to derive plausible annual probabilities for volcanic eruptions. These probabilities were converted to monthly values and used to create time series of the occurrence of random volcanoes with a realistic distribution of size and location based on the two millennia ice core reconstruction.

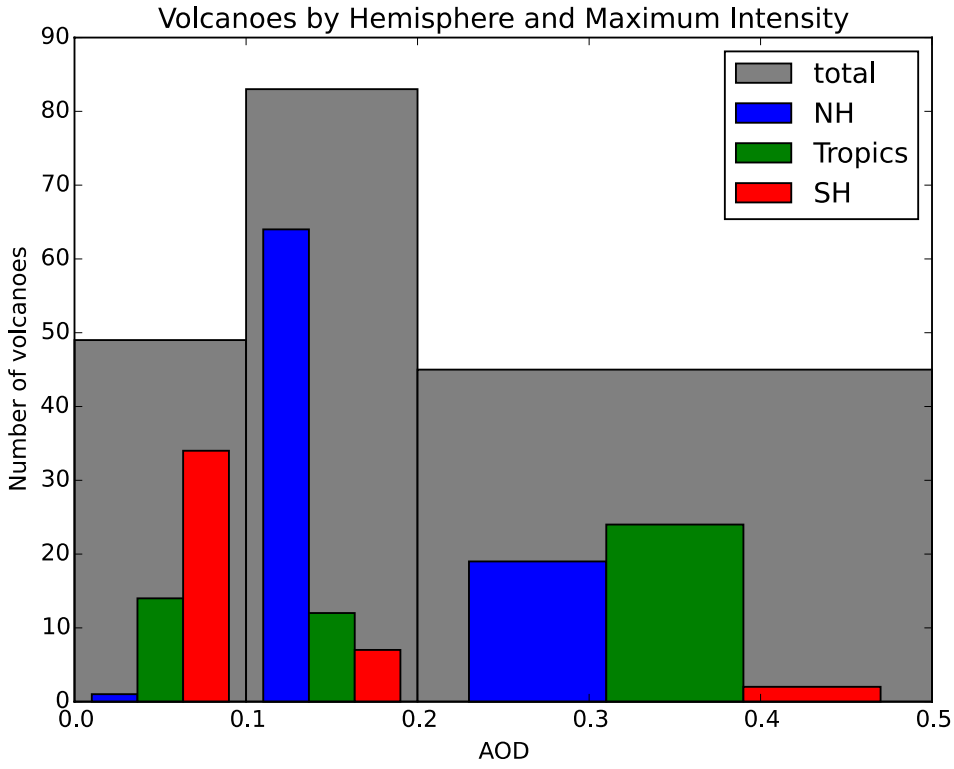

Figure 1: Frequency distribution of historical eruptions. Histogram of volcanoes from Sigl et al. [2013] separated by extra-tropical hemisphere or tropical, and by magnitude band based on peak aerosol optical depth.

The Norwegian Earth System model (NorESM) is a fully coupled global climate model with atmospheric chemistry components. In NorESM, the forcing effect of volcanoes is included through the zonal mass-mixing ratio specified at each latitude and on each vertical level. In practice, the model uses the zonal mean column mass of aerosols distributed over the vertical levels by a simple shape function. The column mass of volcanic aerosols used in NorESM was based on the work of Sato et al. [1993]. The column mass used to drive NorESM in the CMIP5 historical experiment, which covered the period of 1850-2005, was examined and individual volcanoes were identified. These volcanoes were divided into two distinct categories: Tropical and extra-tropical. Since all the volcanoes in the tropical categories had a very similar shape in the historical forcing, a composite mean was created to be a generic example of a tropical volcano in the model. In order to test the quality of the created composite mean volcano, one tropical volcano was randomly left out of the creation of the composite. The

excluded volcano was then correlated to a version of the composite, scaled to be of the same peak magnitude. This was repeated excluding each of the tropical volcanoes in turn. The lowest correlation found was R=0.92 (P<=0.05). This provides good confidence that the composite can be used to accurately represent historical volcanoes as they are represented in NorESM. The process was repeated for extra-tropical volcanoes, with the lowest correlation between scaled-composite and excluded original volcanoes being R=0.94 (p<=0.05).

Synthetic future volcanic forcings for NorESM were then created by inserting the tropical or extra-tropical composites as appropriate into the randomly generated time series. The composites were scaled according to the peak aerosol optical depth. This produced time series of column mass that covered the 21st Century and included volcanoes occurring with the same size and location distribution as was found in the two-millennia ice core records, but with time and latitudinal dispersals that were scaled composites of the volcanoes found in the NorESM CMIP5 historical runs. Two 60-member ensembles of NorESM future projections were then produced to cover the period of 2006-2100. The first used a different synthetic forcing of volcanic eruptions for each ensemble member and was the sensitivity ensemble (SensAll). The second 60-member ensemble served as the reference ensemble (Reference) in which all volcanic forcings were turned off. All other external forcings in both ensembles were set to representative concentration pathway RCP4.5 values as used in the CMIP5 experiments [Vuuren et al. 2011]. The synthetic future volcanic forcings compare well to the forcings found in the CMIP5 Historical run (Figure 2).

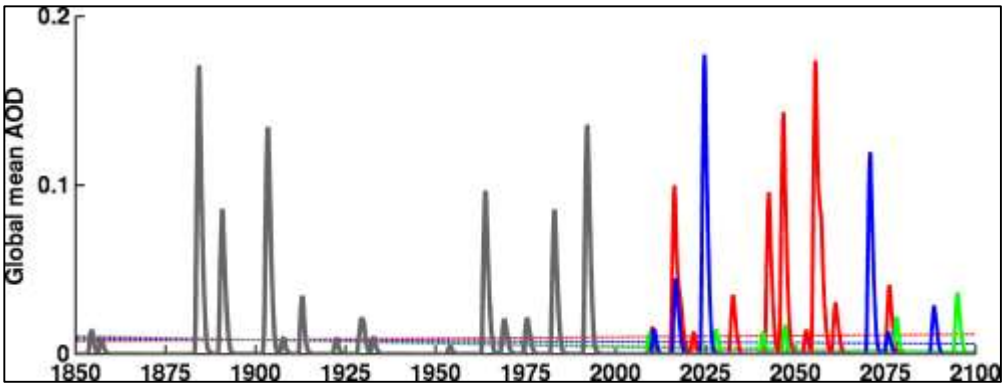

Figure 2: Global mean aerosol optical depth of volcanic forcing used in the Norwegian Earth System Model's historical and 21st century CMIP5 simulations (grey). Synthetic future forcing for the statistical low (5th percentile - green), medium (50th percentile - blue) and high (95th percentile - red) ensemble members. The data is monthly, filtered with a 12-month running mean.

The initial analysis of the results of these simulations has focussed on the global mean surface air temperature – one of the most important climate indicators. Figure 3 shows the global SAT changes over the course of the 21st Century as projected in the Reference and SensAll ensembles. The SensAll ensemble mean is cooler than the Reference ensemble mean in almost all years with the addition of volcanic eruptions resulting in a cooling as expected. The difference is not statistically significant before 2040 when it saturates at around ~0.1 K, after which the differences are significant at the 95% level in most years. Of more interest is the increased ensemble spread in SensAll. The ensemble spread in annual global temperature is approximately 20% larger in SensAll relative to Reference (Figure 3 – red vs. blue shading). Since volcanoes cause cooling of the climate, the increased spread is skewed towards lower temperatures. The increased spread in the ensemble is due to the short-lived nature of the volcanoes, which allows for greater difference between individual members, some of which

will contain volcanoes and some of which will not. The SensAll spread also is uneven in time and roughly mirrors the evolution of the ensemble mean volcanic AOD (Figure 3, bottom), indicating that 60 forcing members are not sufficient for providing a good probabilistic representation on annual resolution. The differences do become more robust when moving towards longer time scales. The decadal mean global temperatures were calculated after removing the global warming trend. The distribution of the decadal means (not shown) is considerably wider in SensAll than in Reference with the frequency of anomalously cold decades increased at the expense of median decades. Similarly, decadal trends also showed an increased frequency towards lower values. As a consequence of the increased occurrence of lower decadal trends, we estimate that decades with zero trend – so-called "warming pauses" – become ~50% more frequent when accounting for volcanic forcing. Investigation is still ongoing to further explore and confirm the impacts of volcanic eruptions on decadal projections.

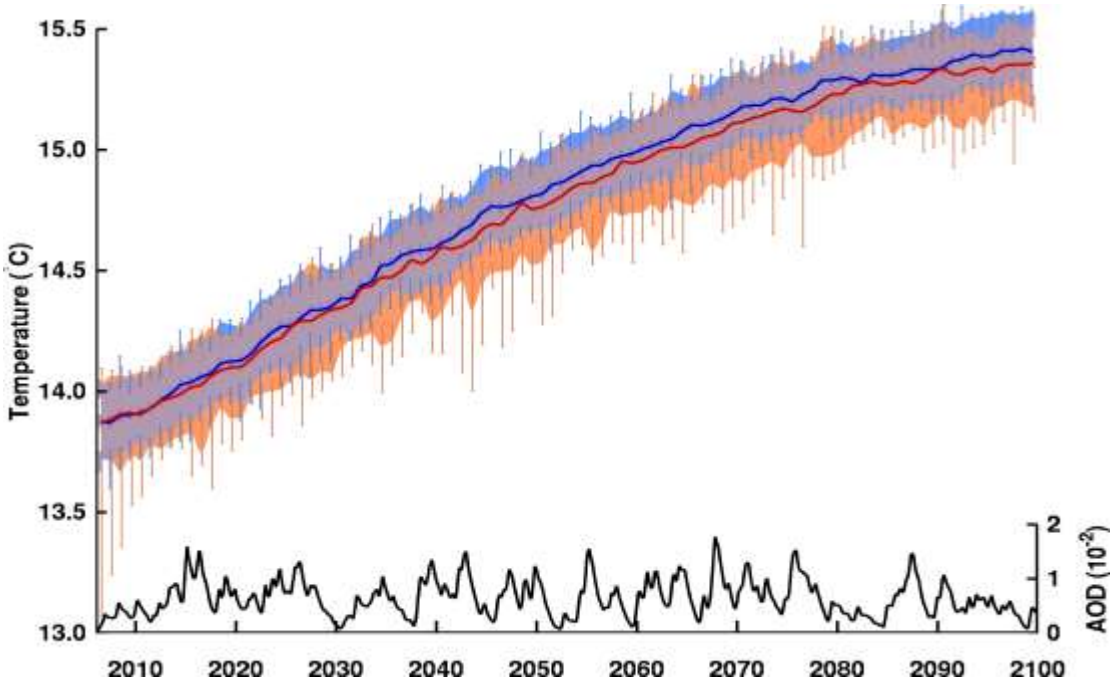

Figure 3: *Top:* Ensemble mean shown as solid line for Reference (blue) and Sensitivity (red) with ensemble spread of 5th to 95th percentiles shown as shading. Bars denote 5-95% bootstrap confidence bounds. *Bottom:* Ensemble mean global mean aerosol optical depth (AOD) of volcanic forcing.

There has been a growing interest in recent years regarding the role of volcanoes in shaping the Earth's climate. This is primarily for climate change attribution and climate geo-engineering [Myhre et al. 2013, Robock et al. 2013], but partly because recent small but persistent volcanoes may have been important in explaining in part the early twentieth Century warming. The possibility of using past knowledge of volcanic eruptions to help improve future projections of climate have so far been largely overlooked. This study has taken a reconstruction of the volcanic activity over the past two millennia and created synthetic future volcanic forcings with plausible distributions of magnitude and geographical spread. Using these, we have shown that the potential impact of excluding volcanoes from climate simulations of the future will likely result in an underestimations of both the inter-annual variability and the occurrence of decades with lower and possibly negative global temperature trends. This work

is currently ongoing with the first publication of this novel method expected later this year [Bethke et al. – in prep]

References

Stenchikov, G. et al. 2006: Arctic Oscillation response to volcanic eruptions in the IPCC AR4 climate models. *J. Geophys. Res.* **111**, D07107

Driscoll, S., Bozzo, A., Gray, L. J., Robock, A. & Stenchikov, G., 2012: Coupled Model Intercomparison Project 5 (CMIP5) simulations of climate following volcanic eruptions. *J. Geophys. Res. Atmos.* **117,** D17105

Stenchikov, G. et al. 2009: Volcanic signals in oceans. *J. Geophys. Res.* **114,** D16104

Otterå, O. H., Bentsen, M., Drange, H. & Suo, L., 2010: External forcing as a metronome for Atlantic multidecadal variability. *Nat. Geosci.* **3,** 688–694

Swingedouw, D. *et al.,* 2015: Bidecadal North Atlantic ocean circulation variability controlled by timing of volcanic eruptions. *Nat. Commun.* **6,** 6545

Sato, M., J. E. Hansen, M. P. McCormaick, and J. B. Pollack, 1993: Stratospheric aerosol optical depths, 18050-1990, *J. Geophys. Res.* **98**, 22,987-22,994

Bethke, I., Outten S., Thorne, P. and Otterå, O. H.: What role for volcanoes in future climate projections? *Nat. Clim. Chang.*, in prep

Arctic Amplification and mid-latitude weather: What can we learn from the early 20th century warming and the current warming period?

Linling Chen

The rise in near-surface air temperatures in the Arctic has been almost twice as large as the global average in recent decades (known as Arctic Amplification (AA)), but cold, snowy winters have been found over mid-latitude land areas. [Bengtsson et al., 2004; Johannessen et al., 2004; Serreze and Francis, 2006; Overland et al., 2011; Serreze and Barry, 2011; Cohen et al., 2012; Greene, 2012]. Similarly, there were some extremely cold winters being documented during the early 20th century warming period [Brönnimann et al., 2004].

Main findings

Atmospheric circulation patterns corresponding to the severe European winters were obtained.

The study identifies statistical relationships between cyclonic-anticyclonic activities and weather conditions in Greenland, and thus concluded that the synoptic activity is a main driver of surface mass balance change during 1980-2013.

Cohen et al. (2012) suggested that winter mid-latitude cooling trends could not be explained entirely by internal variability of the climate system (e.g. North Atlantic Oscillation or the Arctic Oscillation). "What happens in the Arctic does not stay in the Arctic". Several studies suggested a possible link between the Arctic Amplification and the change of weather pattern in the mid-latitude during the current warming period. In particular, Francis and Vavrus (2012) hypothesized that a decrease of the meridional temperature gradients due to AA over the last three decades has led to (a) weakened zonal winds and (b) increased Rossby wave.

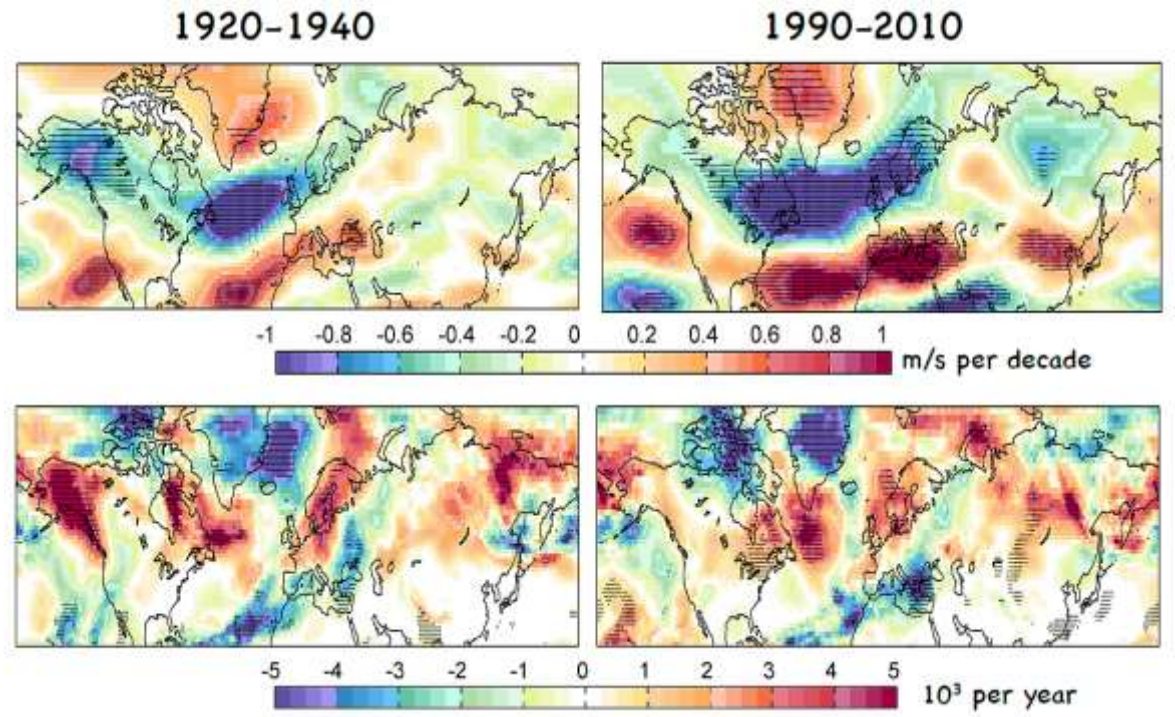

Figure 1 Trends in zonal wind at 500hPa (upper panel) and the absolute value of the MCI (lower panel) during 1920-1940 (left column) and 1990-2010 (right column). The black dots denote statistically significant areas with a 95% confidence. All the analyses are based on ERA20C reanalysis data (http://www.ecmwf.int/en/research/climate-reanalysis/era-20c). This figure is from Chen et al., 2016 (in prep.).

In other words, it has led to a greater north-south meandering of the polar jet stream over North America and the Atlantic Ocean. Larger amplitude waves propagate more slowly than smaller amplitude waves, and therefore favour persistent weather conditions, such as cold spells, heat waves, droughts, and floods in mid-latitudes. However, the robust dynamical feature of this hypothesis is still under debate [Hopsch et al., 2012; Barnes, 2013; Screen and Simmonds, 2013; Barnes et al., 2014; Cohen et al., 2014; Wallace et al., 2014; Barnes and Screen, 2015].

In this study, we analyzed the dynamical features of those severe winters during both warming periods. The purpose is to provide better understanding and long-term perspective of the drivers of SAT variability in the mid-latitude. Fig.1 demonstrated the significant 500hPa zonal winds weakening (upper panel) and wavier flow pattern (lower panel, shown as linear trends of absolute value of the Meridional Circulation Index (MCI) defined by Francis and Vavrus (2012)) during both warming periods. To what extant the changes of these features are caused by AA still needs to be tested.

References

Barnes EA. 2013. Revisiting the evidence linking Arctic amplification to extreme weather in midlatitudes. Geophysical Research Letters 40(17): 4734-4739.

Barnes EA, Dunn- Sigouin E, Masato G, Woollings T. 2014. Exploring recent trends in Northern Hemisphere blocking. Geophysical Research Letters 41(2): 638-644.

Barnes EA, Screen JA. 2015. The impact of Arctic warming on the midlatitude jet- stream: Can it? Has it? Will it? Wiley Interdisciplinary Reviews: Clim. Change 6(3): 277-286.

Bengtsson L, Semenov VA, Johannessen OM. 2004. The early twentieth-century warming in the Arctic-A possible mechanism. J. Climate 17(20): 4045-4057.

Brönnimann S, Luterbacher J, Staehelin J, Svendby T, Hansen G, Svenøe T. 2004. Extreme climate of the global troposphere and stratosphere in 1940–42 related to El Nino. Nature 431(7011): 971-974.

Cohen J, Furtado JC, Barlow MA, Alexeev VA, Cherry JE. 2012. Arctic warming, increasing snow cover and widespread boreal winter cooling. Environ. Res. Lett. 7(1): 014007.

Cohen J, Screen JA, Furtado JC, Barlow M, Whittleston D, Coumou D, Francis J, Dethloff K, Entekhabi D, Overland J. 2014. Recent Arctic amplification and extreme mid-latitude weather. Nature Geoscience 7(9): 627-637.

Francis J, Vavrus S. 2012. Evidence linking Arctic amplification to extreme weather in mid- latitudes. Geophys. Res. Lett. 39(6).

Greene CH. 2012. The winters of our discontent. Scientific American 307(6): 50-55.

Hopsch S, Cohen J, Dethloff K. 2012. Analysis of a link between fall Arctic sea ice concentration and atmospheric patterns in the following winter. Tellus A 64.

Johannessen OM, Bengtsson L, Miles MW, Kuzmina SI, Semenov VA, Alekseev GV, Nagurnyi AP, Zakharov VF, Bobylev LP, Pettersson LH. 2004. Arctic climate change: Observed and modelled temperature and sea- ice variability. Tellus A 56(4): 328-341.

Overland J, Wood KR, Wang M. 2011. Warm Arctic-cold continents: climate impacts of the newly open Arctic Sea. Polar Research 30: 15787.

Screen JA, Simmonds I. 2013. Exploring links between Arctic amplification and mid- latitude weather. Geophys. Res. Lett. 40: 1-6.

Serreze MC, Francis JA. 2006. The Arctic amplification debate. Clim. Change 76(3): 241-264.

Serreze MC, Barry RG. 2011. Processes and impacts of Arctic amplification: A research synthesis. Global and Planetary Change 77(1): 85-96.

Wallace JM, Held IM, Thompson DW, Trenberth KE, Walsh JE. 2014. Global warming and winter weather. Science 343: 729-730.

Climatology of the high-latitude boundary layer and its role in the climate system

Richard Davy and Igor Esau

Here we review the climatology of the atmospheric boundary layer (ABL) at high-latitudes and the representation of the ABL in global climate models. The climatology of the arctic ABL is expected to change dramatically in the coming decades as we move towards a 'blue Arctic' i.e. an Arctic with nearly sea-ice-free conditions in the summer. For example, the presence of sea-ice strongly reduces heat and moisture fluxes between the atmosphere and ocean, and so has a strong influence on the climatology of the ABL over the Arctic basin. As the sea-ice retreats we can expect the heat released from the ocean to lead to enhanced vertical mixing in the atmosphere, and deeper boundary-layers.

Main findings

Global climate models are biased towards over-estimating the amount of mixing under stable-stratification.

This study compared the historical scenarios of CMIP5 with reanalysis data. It shows that the model bias in the temperature variability is relatively small under convective conditions. However, the models tend to under-estimate the temperature variability in stably-stratified conditions.

The depth of the ABL defines the effective heat capacity of the atmosphere, and so determines how much the surface air temperature will change in response to an external forcing [Esau and Zilitinkevich, 2010; Esau et al., 2012]. This can be expressed through an energy-budget model of the atmosphere of the form:

$$\frac{dT}{dt} = \frac{Q}{\rho c_p h} \qquad (1)$$

where Q [W m^{-2}] is the heat input into the boundary layer of depth h [m], with air density ρ [kg m^{-3}] and specific heat capacity c_p [J kg^{-1} K^{-1}] which leads to a change in the representative temperature of the boundary layer, T [K]. This inverse relationship between the temperature response and ABL depth under a given forcing can be seen in the surface temperature tends over recent decades (Figure 1). Under a spatially-uniform forcing, such as that from the build-up of greenhouse gases, it is the locations with the shallowest boundary layers which have warmed the fastest. Thus it is the climatology of the Arctic ABL which is partly responsible for the enhanced warming (Arctic amplification) that has been observed in the Arctic in recent decades. The strongly stable-stratification that is often found over-ice in the Arctic traps the warm air near the surface, and so there has been a more pronounced warming effect in the Arctic than elsewhere.

This amplified response in the surface temperature due to the small effective heat capacity of the atmosphere under stable-stratification can also be seen at different spatial and temporal scales. So for example, we can see night-time temperatures have warmed more rapidly than day-time temperatures, and winter temperatures have increased more rapidly than summer temperatures, under a uniform increase in the global forcing (Figure 2).

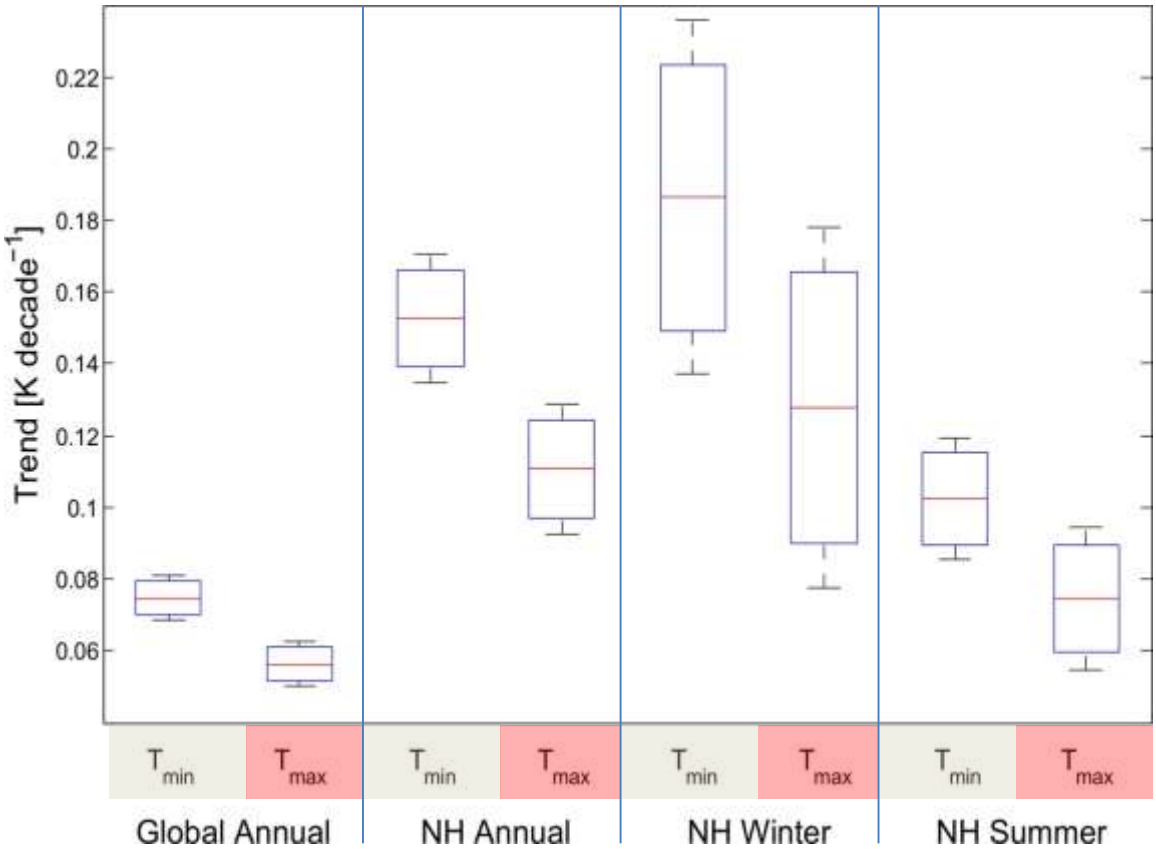

Figure 1. The surface air temperature trend over the period 1979-2010 as a function of the mean boundary layer depth during this period. Data from ERA-Interim.

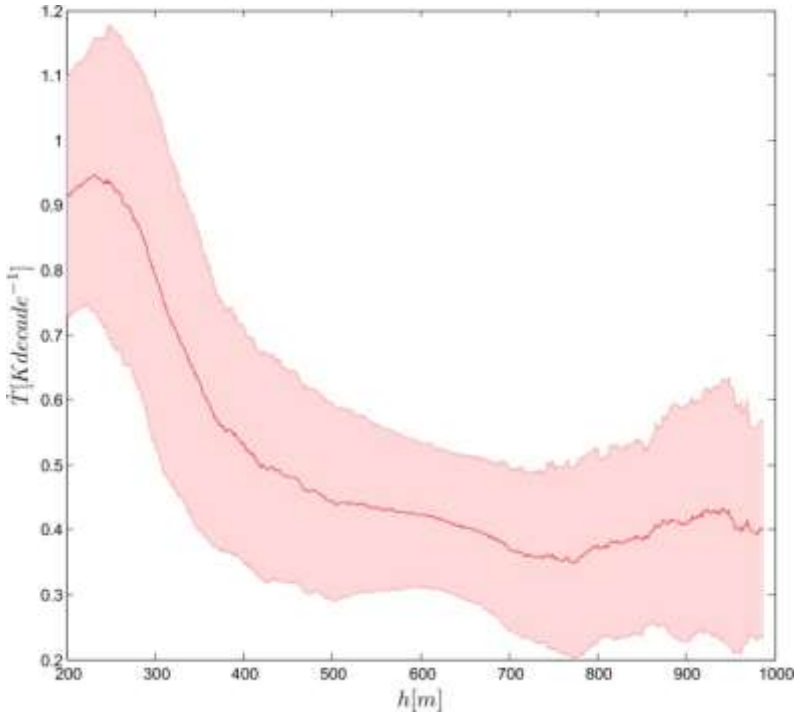

Figure 2. The trends in the diurnal minimum and maximum temperatures over land for the period 1950-2004 from the gridded observations from the Climate Research Unit, CRU TS 3.10. Trends are shown for the global-annual-mean, northern hemisphere (NH) annual-mean and the boreal winter (DJF) and summer (JJA) seasons.

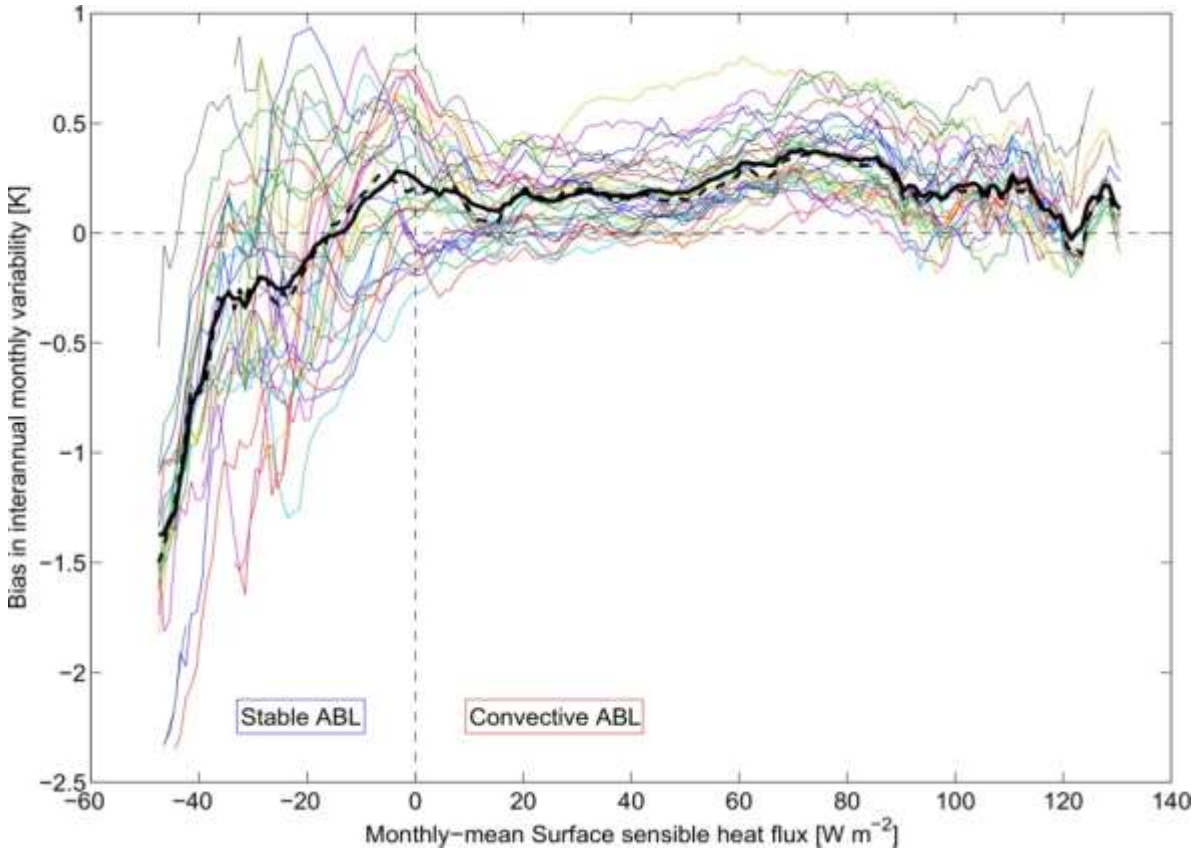

Figure 3. The bias in the interannual surface air temperature variability as a function of surface sensible heat flux from 36 Global Climate Model historical scenarios in CMIP5 in comparison with ERA-Interim over the period 1979-2004.

Global climate models do not capture many of the processes that occur in stable boundary layers, and it has been shown that these models are biased towards over-estimating the amount of mixing under stable-stratification [Seidel et al., 2012; Holtslag et al., 2013; Davy and Esau, 2014]. This has led to a systematic bias in GCMs to under-estimating how much surface temperatures respond to changes in the surface energy budget [Pithan et al., 2013]. This can be seen in comparisons of the historical scenarios of CMIP5 with reanalysis data (Figure 3). The surface sensible heat flux (SSHF) is a good proxy for the state of the boundary layer: for negative heat flux we have a cooling surface and shallow, stably-stratified ABLs. Whereas for strongly positive SSHF we have strong convection, and we find relatively deep ABLs. The model bias in the temperature variability is relatively small under convective conditions, and doesn't vary with the SSHF i.e. the bias is insensitive to the ABL depth. However, as we go towards shallow boundary layers with more negative SSHF we see the models tend to under-estimate the temperature variability. This is consistent with our expectation from the surface energy-budget model (equation 1).

References

Esau, I., and S. Zilitinkevich, 2010: On the role of the planetary boundary layer depth in the climate system. *Adv. Sci. Res.*, **4**, 63-69.

Esau, I., R. Davy, and S. Outten, 2012: Complementary explanation of temperature response in the lower atmosphere. *Environ. Res. Lett.*, **7**(4), 044026.

Pithan, F. and T. Mauritsen, 2013: Arctic amplification dominated by temperature feedbacks in contemporary climate models. *Nature Geosci.*, **7**, 181-184.

Seidel, D.J., *et al.*, 2012: Climatology of the planetary boundary layer over the continental United States and Europe. *J. Geophys. Res.* **115**, D16113.

Davy, R., and I. Esau, 2014: Global climate models' bias in surface temperature trends and variability. *Environ. Res. Lett.*, **9**, 114024.

Holtslag, A.A.M., *et al*., 2013: Stable atmospheric boundary layers and diurnal cycles: challenges for weather and climate models. *B. Am. Meteor. Soc.*, **94(**11), 1691-1706.

Chaotic atmospheric systems: Response theory and methods for constructing response operators

***Andrey Gritsun*[1,*]**

[1] Institute for Numerical Mathematics, Moscow, Russia
* Solicited guest lecture

Main findings

The study considers asymptotic behavior of some conceptual models of the chaotic atmospheric system. A new statistical method to reconstruct the model response operators is proposed and discussed.

It is shown that barotropic T21 system has (infinitely?) many periodic orbits. Least unstable orbits are important for explaining model variability patterns (especially CEOFs). Response theory works well for barotropic T21: response is linear well beyond "smallness" assumption; response could be recovered from single forcing

After Lorenz's discovery of deterministic chaos [Lorenz, 1963], dynamical system theory has played an increasing role in the theory of climate. The widely accepted fact now is that a typical atmospheric system, like the famous Lorenz-63 model, is dissipative (i.e. it is contracting in phase space) and chaotic (system trajectories are sensitive with respect to initial conditions). The system energy is bounded and it evolves in a bounded set. These two facts guarantee (for finite-dimensional systems) the existence of a nontrivial invariant attracting fractal set inside the system phase space. Many atmospheric systems have such an attractor. An important property of an attractor is that a stationary probability distribution function could be defined on it, and therefore, it allows averages along system trajectories as well as other statistical characteristics of the system, which gives a strong theoretical basis for climate modeling. On Fig.1 one can see an illustration of this type of behavior – ensemble of states becomes time independent after some evolution time.

The dynamical system theory studies the asymptotic system behavior in the vicinity of an attractor and provides important information about the system. Lyapunov exponents (local and global) give the measure of instability of system trajectories; attractor dimension is a general measure for the complexity of system dynamics; information entropy is a useful tool for analyzing PDFs on the system attractors, etc. The next logical step in understanding and quantifying attractors of atmospheric models would be construction of the corresponding PDF, giving all information about system statistical characteristics. Unfortunately these attractors are fractals having large dimensionality so it is not possible to perform this sort of calculation directly. One of these methods is based on so-called unstable periodic orbits (UPOs) expansion. According to it, the system measure (or its statistical characteristics) is approximated as a weighted sum over the orbits. The weights are inversely proportional to the orbit instability characteristics so that the least unstable orbits make larger contributions to the PDF. The strong chaoticity (hyperbolicity or Axiom A property) of the system is usually required for this method to be theoretically justified [Ruelle, 1999; Katok and Hasselblatt 1996]. For such systems the set of periodic orbits is dense on the attractor of the system and the explicit expression for the system invariant measure via UPO expansion could be obtained. As a result, any arbitrary trajectory of the system can be approximated with any prescribed accuracy by these periodic orbits and all system statistical characteristics (including the probability to find the system trajectory near a given state) could be calculated using UPOs. First application of this UPO-expansion strategy was performed in [Auerbach et.al, 1987] for the simplest dynamical system.

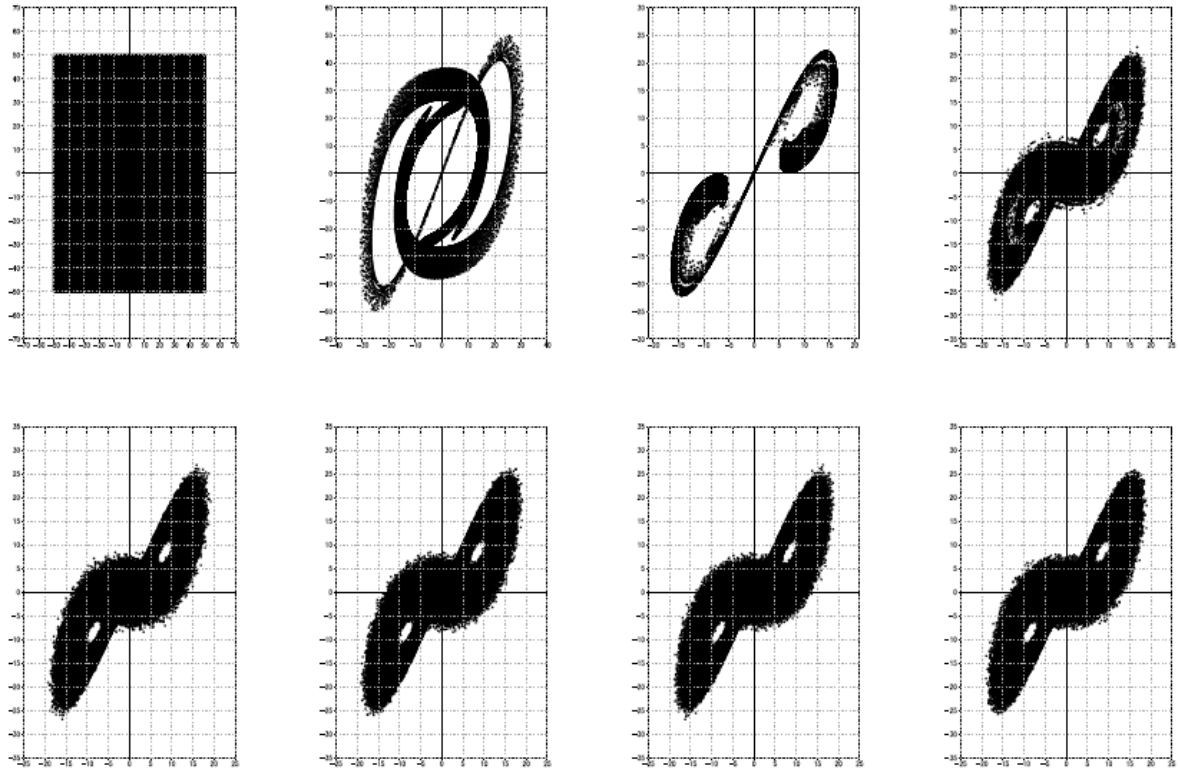

Figure 1 Evolution of the 1 million point ensemble of Lorenz system.

For the systems of atmospheric dynamics it is not possible to verify the hyperbolicity assumption, and, more likely, atmospheric models belong to the wider class of dynamical systems - systems with nonzero Lyapunov exponents. In turns, the generalization of the UPO expansion theory for systems with nonzero Lyapunov exponents has not yet been obtained. Following the ideas of Gallavotty ("chaotic hypothesis", [Gallavotti and Cohen, 1996]) one may suppose that the typical multidimensional chaotic systems behave like Axiom A systems, at least if one wants to calculate their macroscopic (average) characteristics, and apply the UPO expansion numerically. The study of applicability of this approach for typical climate systems is an ongoing research. We will show how it is working for simple barotropic model of atmosphere (description of the model could be found in [Gritsun, 2008]).

By the definition, a periodic orbit with the period *T* is a system trajectory returning into the same position in the phase space after time *T*. Write the system equation in the resolved form $\psi(t) = S(t,\psi_0)$. As a result, we get equation (system is supposed to be autonomous) for UPO trajectory $\psi(T) = S(T,\psi_0) = \psi_0$ that is indeed a system of nonlinear equations with respect to the initial position of the orbit and its period (as initial position of the system and integration time uniquely define the system trajectory). Numerical methods for finding UPOs solve this system with one or another method (see [Gritsun, 2008] for details).

The UPOs of the system are embedded into the system attractor and the system trajectory evolves in the phase space passing from one orbit to another. As a result, UPOs may approximate the system trajectory to some extent. The idea of the approximation is to replace the averaging along the trajectory by the averaging along the orbits. From the physical point of view it is clear that the orbits visited by a system trajectory more frequently must have larger weights w_i in this approximation. Consequently, we obtain approximation formula that looks

almost the same as traditional (trajectory) averaging formula but the "measurement" weights are different from orbit to orbit.

$$< F > \approx \frac{1}{W} \sum_{i=1}^{I(T)} w_i F(\psi^i)), \quad W = \sum_{i=1}^{I(T)} w_i .$$

For the Axiom A systems this procedure could be theoretically justified [Ruelle, 1999; Katok and Hasselblatt, 1996]. According to this theory [Ruelle, 1999] weights w_i must be calculated as $w_i = 1/\exp(T\sum_j \lambda_j^{i+})$, where λ_j^{i+} are positive Lyapunov exponents of the orbit containing i-th periodic point so least unstable orbits make more contribution to the average. Result of this calculation for barotropic T21 model is presented on Fig.2. Top planes show PDF projections of the model streamfunction on leading EOF planes. One can see that with UPO averaging one can obtain really good get approximations (bottom plane). The same conclusion could be derived for other statistical characteristics of the model (i.e. average state, variability patterns, attractor dimension, Lyupunov exponents, probability of the system to be inside a given set etc).

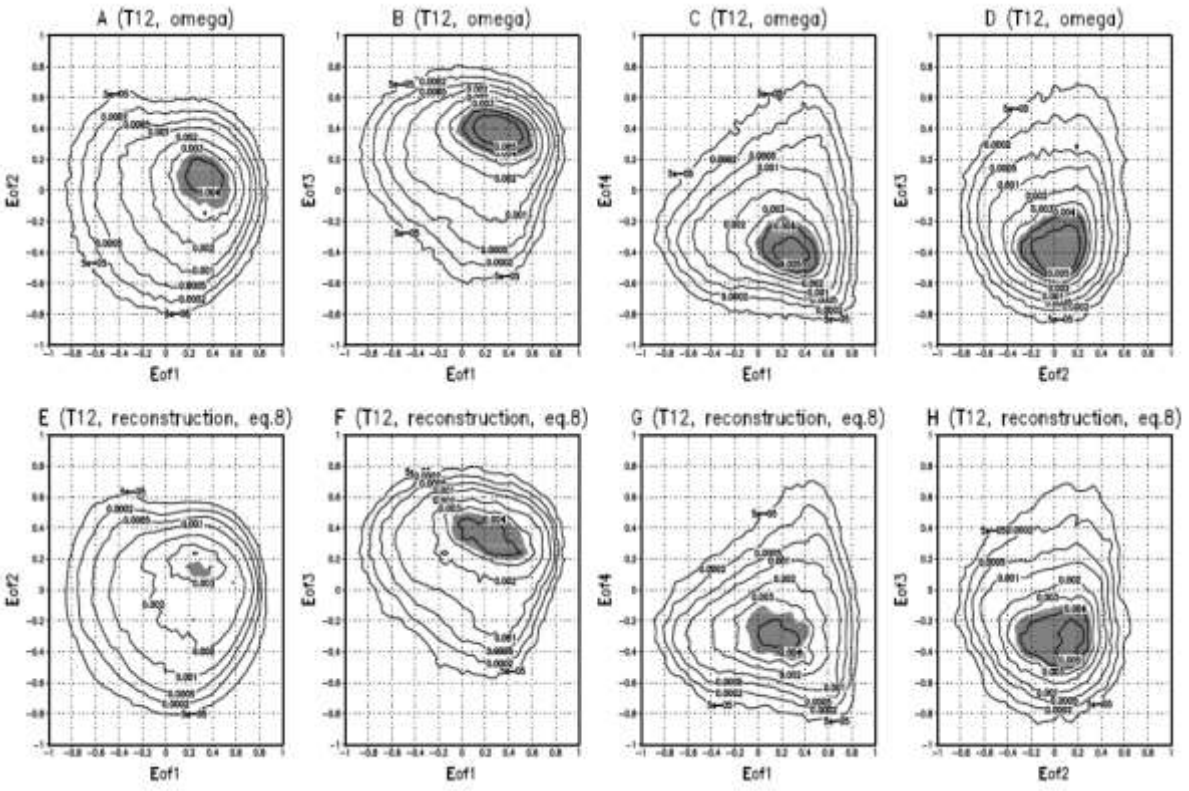

Figure 2. Top – PDF projections for the barotropic model streamfunction: A) EOF1-EOF2 plane; B) EOF1-EOF3 plane; C) EOF1-EOF4 plane; D) EOF2-EOF3 plane. Bottom – PDF projections reconstructed using UPOs.

Another mathematical tool coming from Axiom A theory and being important in the climate research is a response theory. In many important cases one can define a linear dependence between the small changes of external forcing acting on the system and its statistical characteristics (the so-called response operator). The knowledge of the response operator gives all the information about system sensitivity with respect to the external perturbations. Let us apply a small perturbation to the system right hand side resulting in changes of the system invariant measure and statistical characteristics

It can be shown that, up to the second order of the forcing term, the system response could be obtained as

$$\mu \to \mu_\varepsilon(t) \quad \overline{A} \to \overline{A}_\varepsilon(t)$$

$$\delta A_\varepsilon(t) = \overline{A} - \overline{A}_\varepsilon = \varepsilon \int G_1(\tau) g(t-\tau) d\tau + \varepsilon^2 \iint G_2(\tau_1, \tau_2) g(t-\tau_1) g(t-\tau_2) d\tau_1 d\tau_2$$

$$G_1(\tau_1) = \int d\mu \Theta(\tau_1) \delta f_i \partial_i A(f(S(\tau_1, x))) / \partial x_i$$

(Chaotic hypothesis assumption and smallness of the perturbation is required here). As a result, response of the system to the forcing pattern δf with amplitude $g(t)$ could be obtained from the response with amplitude $g_1(t)$ [Lucarini, Sarno, 2009]. In particular,

$$g(t) = \delta(t) \to \delta A_{\varepsilon,\delta}(t) = \varepsilon G_1(t)$$
$$g(t) = \Theta(t) \to \delta A_{\varepsilon,\Theta}(t) = \varepsilon \int G_1(\tau) d\tau$$
$$\delta A_{\varepsilon,\Theta}(t) = \int \delta A_{\varepsilon,\delta}(\tau) d\tau$$

This equality holds for the barotropic model to the very high accuracy. On Figure 3 one can see that the response of the system to the constant in time forcing pattern (20% change of the orography) could be in fact obtained as an integral from the system response to the one time step perturbation.

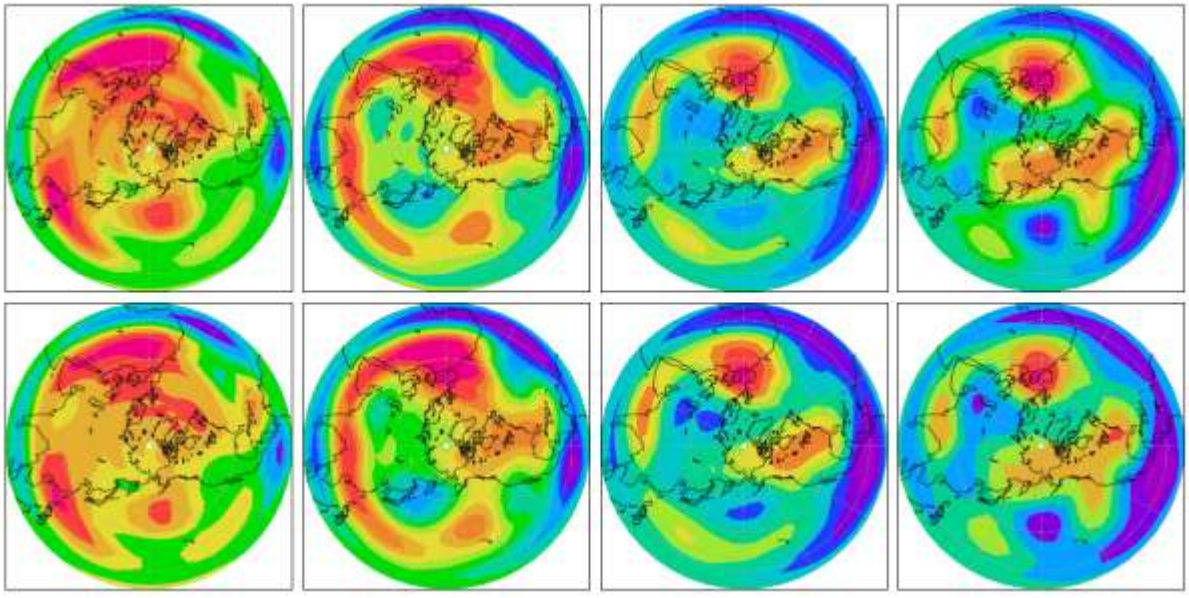

Figure 3. Top – change of the average state of barotropic model under constant in time perturbation $g(t) = \Theta(t)$ (days 2,4,8,12). Bottom - $\int_o^T \delta A_{\varepsilon,\delta}(\tau) d\tau$ (T=2,4,8,12 days). 15000 member ensembles are used to calculate both response functions.

In some case, the power spectrum of the response function could have unexpected maxima indicating resonant behavior of perturbed system. For example, power spectrum of the barotropic system response to the 20% change of the orography (Fig.4, right) has profound

maximum at approximately 2.8 days while equilibrium power spectrum does to have this feature (Fig.4, left). Perturbed system shows well defined oscillation in two-dimensional plane associated with the structures shown on Fig.5. System tendencies projected on this plane (Fig.5, right) illustrates this one more time suggesting quasi-periodic motion of perturbed ensemble. This behavior could be explained by the fact that unperturbed system has many very unstable orbits having the same shape an period (Fig.6). Forcing (change of the orography) kicks the system to this resonant plane and system trajectories has to rotate around these orbits relaxing to the equilibrium ensemble. This resonant behavior of the perturbed system cannot be seen in equilibrium power spectrum as these 2.8 day UPOs are very unstable and the trajectory of unperturbed system has very low chance to be in this region of the phase space.

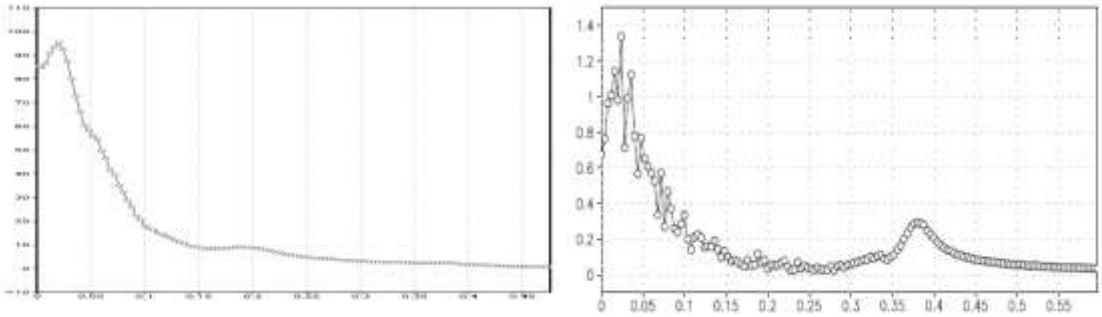

Figure 4. Equilibrium power spectrum of barotropic system (kinetic energy) (left) and power spectrum of the response function to the step forcing.

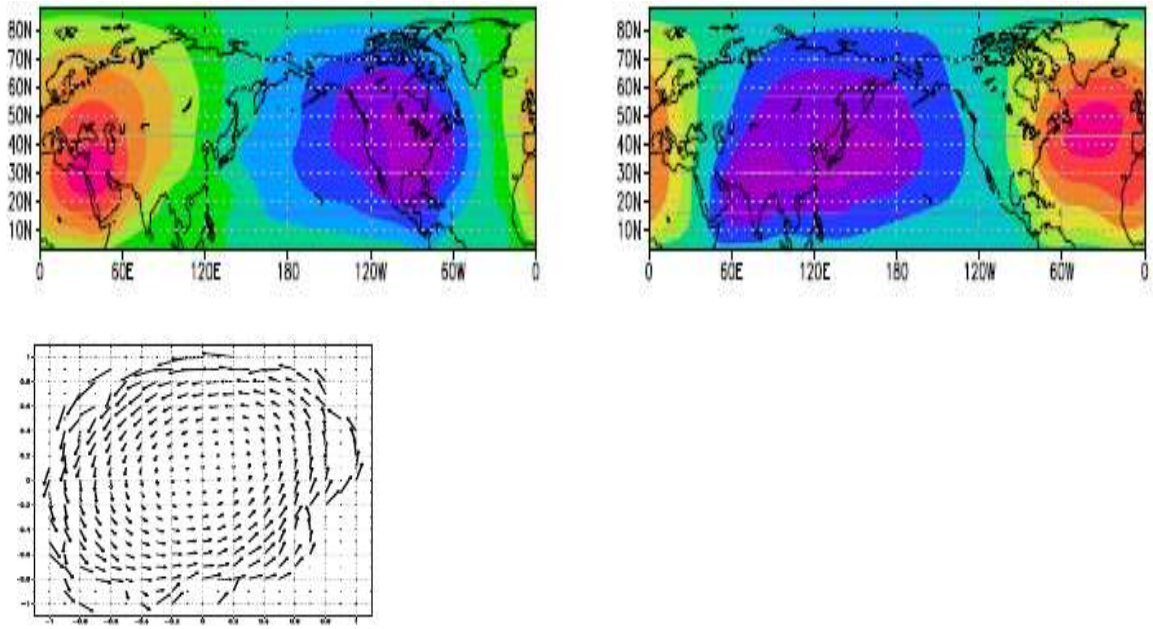

Figure 5. Resonant 2.8 day mode and system tendencies projected onto this plane (below).

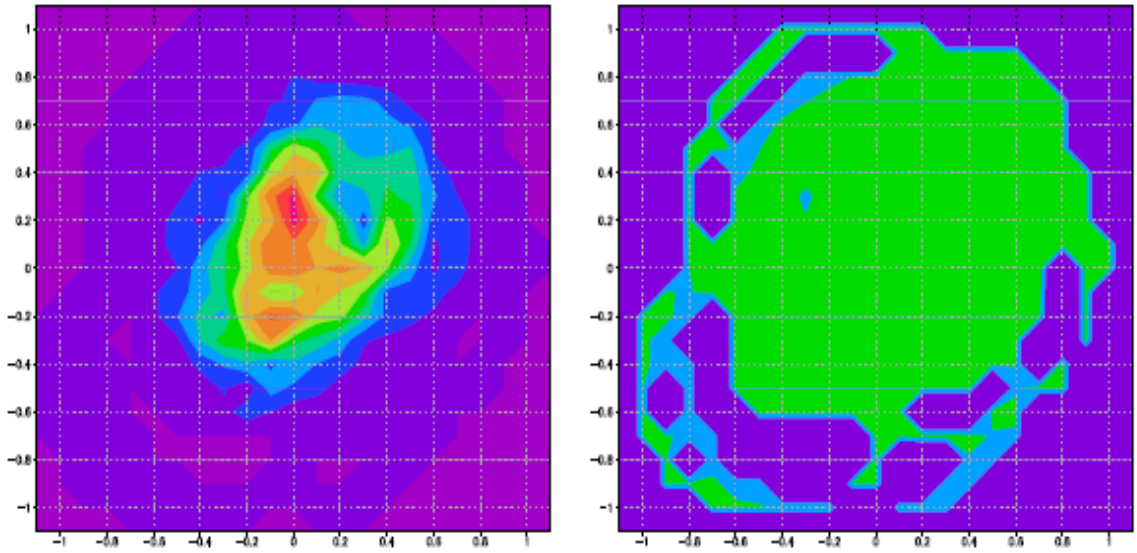

Figure 6. Distribution of UPOs projected onto resonant plane and distribution of corresponding periods (purple – less than 2 days, blue – 2-2.5 days, green 2.5-3 days)

References

Lorenz, E., 1963, Deterministic nonperiodic flow, J. Atmos. Sci., 20, 130-141.

Gallavotti, G., Cohen, E. G. D., 1995, Dynamical ensembles in nonequilibrium statistical mechanics. Physical Review Letters, 74(14), 2694–2697.

D. Ruelle, 1999, Smooth dynamics and new theoretical ideas in nonequilibrium statistical mechanics. J. Statist. Phys., 95, 393–468.

D. Auerbach, P. Cvitanovic, J.-P. Eckmann, G. Gunaratne, I. Procaccia, 1987, Exploring chaotic motion through periodic orbits, Phys. Rev. Lett., 58, 2387–2389.

Gritsun A., 2011, Connection of periodic orbits and variability patterns of circulation for the barotropic model of atmospheric dynamics, Doklady Earth Sciences, 438 (1), 636–640.

Gritsun, A. S., 2008, Unstable periodic trajectories of a barotropic model of the atmosphere. Russian Journal of Numerical Analysis and Mathematical Modelling, 23(4).

V. Lucarini, S. Sarno, 2011, A Statistical Mechanical Approach for the Computation of the Climatic Response to General Forcings, Nonlin. Proc. Geophys. 18, 7.

Cloud types' climatology of the Barents Sea region in context of the convective cloud fields

Alexander V. Chernokulsky[1] and Igor Esau

[1] A.M. Obukhov Institute for Atmospheric Physics, Moscow

Convective cloudiness in the Atlantic sector of the Arctic is considered as an atmospheric spatially self-organized convective field. Convective cloud development is usually studied as a local process reflecting the convective instability of the turbulent planetary boundary layer over a heated surface. The convective cloudiness has a different dynamical structure in high latitudes. Cloud development follows cold-air outbreaks into the areas with a relatively warm surface. As a result, the physical and morphological characteristics of clouds, such as the type of convective cloud, and their geographical localization are interrelated. It has been shown that marginal sea ice and coastal zones are the most frequently occupied by Cu hum, Cu med convective clouds, which are organized in convective rolls. Simultaneously, the open water marine areas are occupied by Cu cong, Cb, which are organized in convective cells. An intercomparison of cloud statistics using satellite data ISCCP and ground-based observations has revealed an inconsistency in the cloudiness trends in these data sources: convective cloudiness decreases in ISCCP data and increases in the ground-based observation data. In general, according to the stated hypothesis, the retreat of the sea-ice boundary may lead to increase in amount of convective clouds.

Main findings

It has been observed that convective cloud forms appear in high Arctic as a dynamical phenomenon tightly linked to the cold air outbreaks.

The proposed convective cloud field hypothesis suggests that the observed changes in the convective clouds could manifest the changes in the atmospheric circulation and large-scale sea ice cover in the Arctic. The analysis reveals increasing convective cloudiness consistent with sea ice cover retreat in the area.

Let us now consider changes in characteristics of cloudiness (primarily the convective one) using the ground-based observation data for the region. The hypothesis of spatially coherent changes in cloudiness implies that the observed convective cloudiness should depend on the position of sea-ice boundary relative to the station and the dynamics of cyclone activity in the region. These two factors are supposed to be interrelated as well [Honda et al., 2009; Outten and Esau, 2011].

Figure 1 represents the climatology of part of the sky (measured in %) covered by convective clouds (n_{Cu+Cb}) (convective cloud amount) using the ground-based observation data for two groups of stations: the ones placed along the sea-ice boundary and the ones placed along the southern coast of Barents and Kara seas. The climatology is generally presented in the west–east direction. It can be easily seen that the maximum n_{Cu+Cb} values are observed at stations of the eastern part of the Barents Sea, where the flow is directed under cold air outbreaks in the rear of the cyclone rather than at the western stations, where the water temperature is the highest. In general, the area of maximum n_{Cu+Cb} values and the maximum repeatability of cumulus cloudiness forms (not indicated) agrees well with the area of frequent cold air outbreaks based on the results of the analysis [Kolstad et al., 2009]. In addition, the maximum n_{Cu+Cb} values and maximum occurrence of cumulus cloudiness along the sea-ice boundary shift

westward from autumn (the maximums at Cape Mikulkin–Kolguev stations) to winter (the maximums at Cape Kanin Nos–Shoyna stations) (n_{Cu+Cb} reaches 30% in some years). At the same time, n_{Cu+Cb} values above ice stations mostly do not exceed 2–5% (only reaching 10% in some years).

The increase in nCu + Cb above the open water is noted in all seasons according to the ground-based observations (Fig. 2). At the same time, the satellite data show the decrease in the amount of convective clouds. The satellite data-based trends of convective cloudiness agree well with negative trends of sensible heat fluxes in the region and the decrease in wind speed, especially in the seasonal sea-ice boundary area. The decrease in the amount of stratus clouds and increase in the amount of convective cloudiness are also accompanied by changes in distribution function of days with different cloudiness conditions: the decrease in the number of overcast days (cloud coverage of the sky is 100%) and the increase in the number of days with broken clouds (cloud coverage of the sky is 50–100%) are observed under weak changes in the total amount of cloudiness. These features are noted for both Russian and Norwegian ground stations and are mostly characteristic of the stations near open water.

The cloud field (CF) hypothesis explains well the difference in cloudiness trends for the stations near the open water and the sea-ice boundary. Indeed, convection always develops similarly in case of cold-air outbreaks. Therefore, changes near the sea-ice boundary are relatively small and are solely due to the frequency of cold-air outbreaks. In the meanwhile, the cloudiness development above the open water depends on heating time of an air particle, i.e., on the distance travelled above the water and wind speed. Since the ice has retreated significantly in recent decades, especially in winter [Zygmuntowska et al., 2014], stronger cumulus cloudiness was now able to develop [Palm et al., 2010]. It may be assumed that water-vapor emission to higher atmospheric layers via convective motion leads to the formation of upper level cloudiness, which partially interferes with recognizing cumulus clouds in satellite imagery.

The proposed CF hypothesis, namely the simultaneity (be it exact or with a certain time delay) of appearance of cumulus clouds in different geographical regions, requires additional analysis. The latter has some difficulties related to the identification of local cloudiness as a part of a unified dynamically connected CF. Kolstad et al. (2009) studies the climatology of cold_air outbreaks in the region in 1958–2007 based on a large-scale meteorological indexing. However, convective cloudiness development in such outbreaks is not considered. Similarly to the cloudiness observation data, the southern part of the Barents Sea is recognized as a region with high frequency of cold outbreaks, but with no significant trend of this frequency. This mismatch between the dynamic and the cloudiness trends may indicate the crucial role of the sea-ice boundary position just as it follows from the CF hypothesis. One of the most important and, at the same time, contradictory results of the statistical analysis of cloudiness may be explained from the perspective of the CF hypothesis. The occurrence of cumulus cloud forms from ground-based observations increases throughout the whole observation history, whereas the satellite data show the decrease in the occurrence of these cloud forms. The trend in the satellite data agrees with the decrease in sensible heat fluxes above the open water in the region, and the trend in ground-based observations agrees with the retreat of the sea-ice boundary. The latter dependence has been established more reliably than changes in fluxes, which have opposite directions in different sources of climatic data.

To conclude, it is necessary to note that cumulus cloud forms are a reliable indicator of convective instability in the lower atmosphere, and since the theory behind this instability is well developed, they allow to obtain information on heat and vapor exchange with the underlying water surface. The appearance of clouds in a spatially organized CF makes it possible to calculate the heat balance on the surface above the whole region. It is especially

important that this method of calculating the balance does not involve interpolating the measurements at separate and often weakly correlated points, but rather relies on physical laws of turbulent convection development.

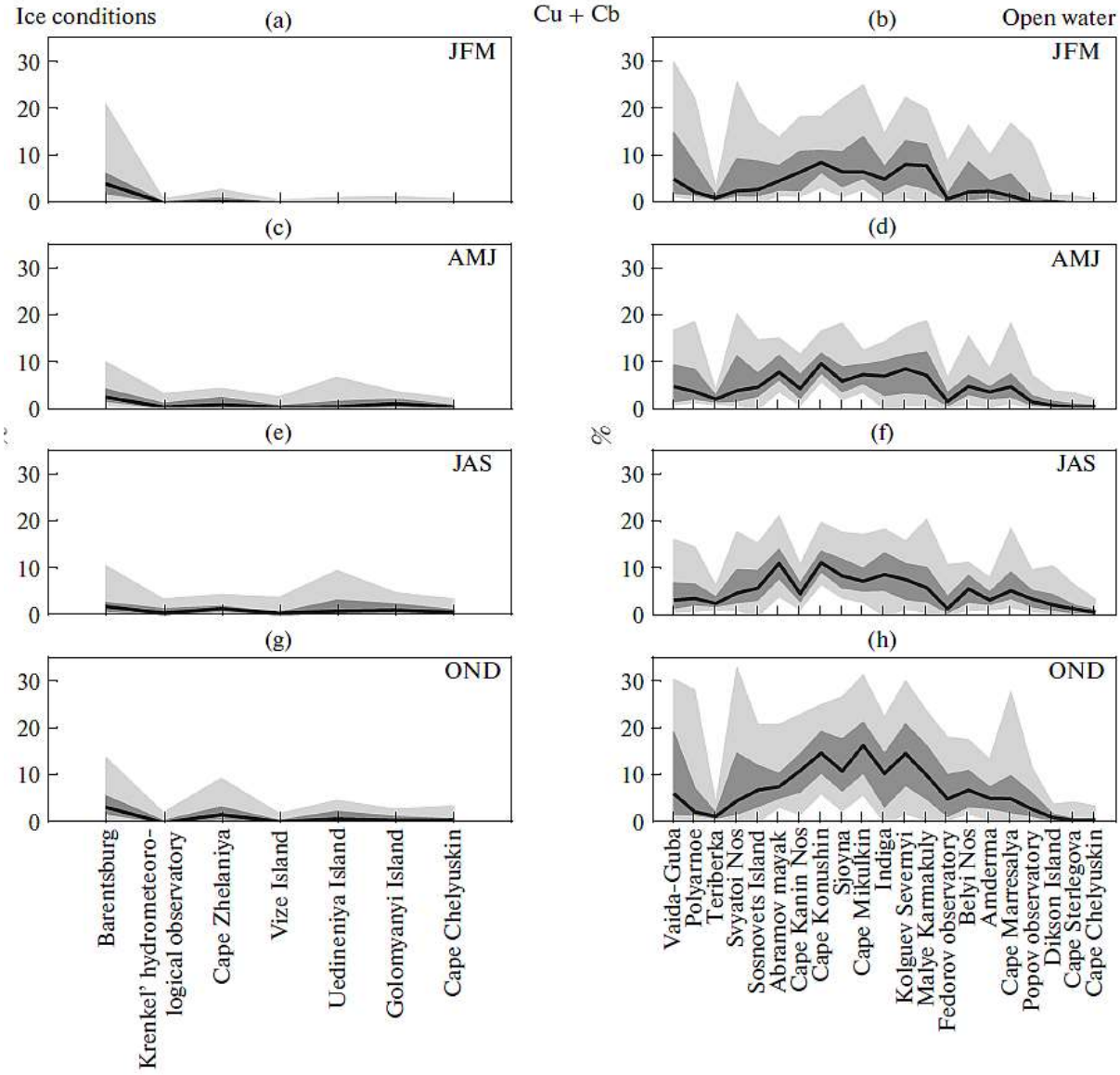

Figure 1. Climatology (1936–2013) of convective clouds (cumulus clouds Cu and cumulonimbus clouds Cb) amount n_{Cu+Cb} according to the ground observation data at stations near the seasonal sea ice boundary (a, c, e, g) and near the southern coasts of Barents and Kara seas (b, d, f, h) in different seasons: January–February–March (a, b), April–May–June (c, d), July–August–September (e, f), and October–November–December (g, h). The black line corresponds to the second quartile, the dark gray area is limited by the first and the third quartiles, and the light gray area is limited by 5th and 95th percentiles of n_{Cu+Cb}. The so-called upper estimates of n_{Cu+Cb} are presented in the plot.

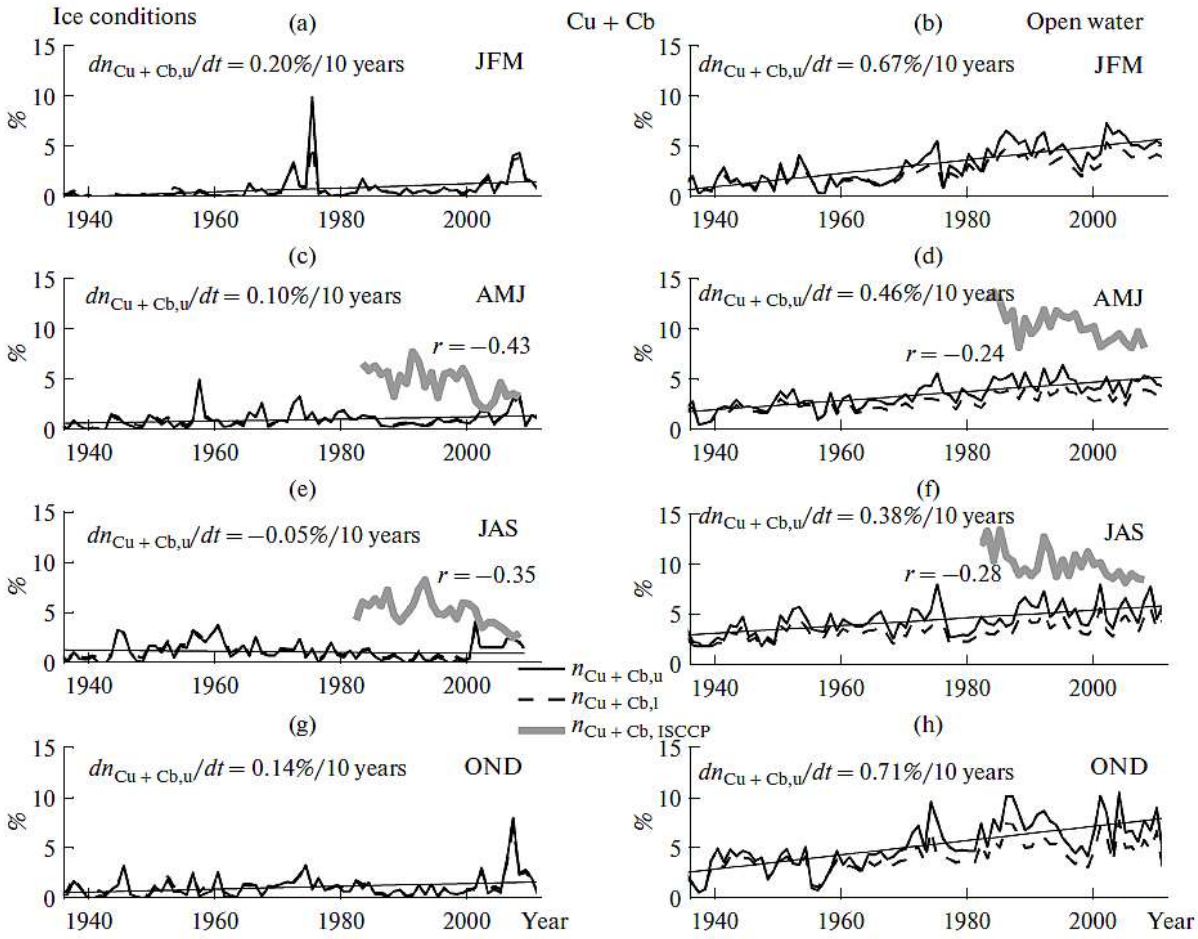

Figure 2. Year-to-year changes in the amount of the sky covered by stratus cloud forms n_{Cu+Cb} according to the ground observation data (black lines, the solid black line is the upper estimate, and the dotted line is the lower estimate) and ISCCP satellite data (gray line, only for the daylight time of the year) averaged for regions of seasonal sea-ice edge (a, c, e, g) and southern boundary of Kara and Barents seas (b, d, f, h) in different seasons: January–February–March (a, b), April–May–June (c, d), July–August–September (e, f), and October–November–December (g, h). Averaging by stations was first performed within the 10° longitudinal sectors (all stations in one sector with equal weights), then average sectoral values were averaged between each other (all sectors with equal weights), and satellite data were averaged by regions corresponding to station positions. Values of the linear trend n_{Cu+Cb}, u, and the correlation coefficient between n_{Cu+Cb},u and n_{Cu+Cb}, ISCCP are shown in the plots as well.

References

Honda, M., Inoue, J., and Yamane, S., Influence of low arctic sea_ice minima on anomalously cold Eurasian winters, *Geophys. Res. Lett.*, 2009, 36, L08707. Doi: 10.1029/2008GL03079

Kolstad, E.W., Bracegirdle, T.J., and Seierstad, I.A., Marine cold_air outbreaks in the north Atlantic: Temporal distribution and associations with large-scale atmospheric circulation, *Clim. Dyn.*, 2009, 33, 187–197.

Outten, S. and Esau, I., A link between Arctic sea ice and recent cooling trends over Eurasia, *Clim. Change*, 2011, 110, 1069–1075. doi 10.1007/s10584-011-0334_z

Palm, S.P., Strey, S.T., Spinhirne, J., and Markus, T., Influence of Arctic sea ice extent on polar cloud fraction and vertical structure and implications for regional climate, *J. Geophys. Res.*, 2010, 115, D21209.

Zygmuntowska, M., Rampal, P., Ivanova, N., and Smedsrud, L.H., Uncertainties in Arctic sea ice thickness and volume: New estimates and implications for trends, *The Cryosphere*, 2014, 8, 705–720. Doi:10.5194/tc-8-705-2014

Chapter 2. Small-scale climate dynamics

Impact of cyclonic and anticyclonic activities on the Greenland Ice Sheet surface mass balance variation during 1980-2013

Linling Chen

Main findings

The study identifies statistical relationships between cyclonic-anticyclonic activities and weather conditions.

The Greenland Ice Sheet (GrIS) has experienced dramatic ice loss during recent decades, but the drivers of the surface mass balance (SMB) variation remain unclear. From a dynamical perspective, extratropical cyclones and anticyclones are the major systems influencing Greenland weather conditions. Seasonal cyclonic and anticyclonic activities have been quantified for the area of 50°-90°N, 80°W-10°E during 1980-2013 by using RV850 as a measure. This created a useful basis for further investigation on the role of synoptic weather in determining the changes of snow accumulation (SA) and surface air temperature (SAT) over the GrIS. This, in turn, helps us to better understand the drivers of the GrIS SMB variability, which has strong impacts on the GrIS mass budget and global sea level change. SVD analysis was used to identify the coupled patterns between the synoptic activities and the SA /SAT over Greenland.

The SA-related CAI patterns derived from the S1 and S2 modes illustrate the activity of cyclones approaching Greenland: 1) from the south, diverted northeastwards to skirt the east coast of Greenland; 2) from the west, passing over Baffin Bay; and 3) from the north, via the Arctic Ocean. The SMB inter-annual variability is well explained by these patterns in southern and northwestern Greenland, where we found the largest and second-largest amount of annual SA. There are no significant phase changes in most of these CAI patterns. However, the JJA CAI pattern derived from the leading SVD mode shows more frequent occurrence of the negative phase since 2005. This suggests a contribution of cyclonic activity to JJA GrIS mass loss by reducing the amount of SA.

The SAT-related CAI or ACAI pattern indicates that less snowy weather or cloud-free conditions along the Greenland coast since 2000 has likely contributed to the accelerated surface mass loss from the GrIS by increasing the JJA SAT. Since the positive phase of the SAT-related ACAI pattern seems consistent with the spatial pattern of the negative phase of the AO/NAO and the positive phase of the GBH, our results suggest that the SAT-related synoptic pattern may influence the SAT by interacting with the permanent large-scale atmospheric center of action over Greenland, which favors warm air advection from the south and along western Greenland. However, subsequent studies are needed to improve the mechanistic understanding of this interaction. These patterns account for up to 80% of the annual SMB variations along the west and northwest coast of Greenland, where significant surface mass loss has been observed over the last decades.

The statistical relationships identified here highlight the important roles of cyclonic and anticyclonic activities in determining weather conditions to favor the changes in SA, SAT and SMB. Further investigation on whether the occurrence of these patterns is mainly due to natural variability, and whether the phase change of these patterns results from global warming, will strengthen the understanding of the past and future SMB change from a longer-term perspective.

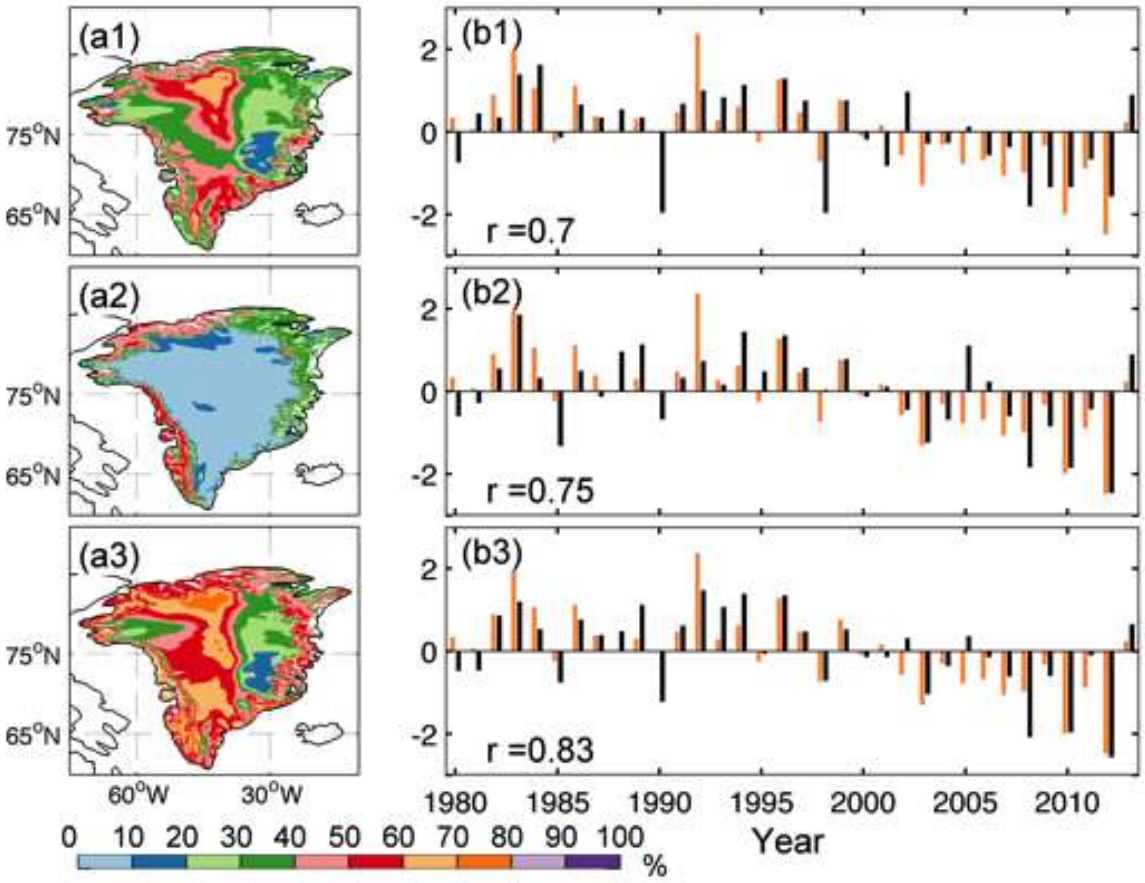

Figure 1. The spatial distribution of r2 statistics from: (a1) the regression between the SMB and the expansion coefficients of CAI field identified from the S1 and S2 modes; (a2) the regression between the SMB and the expansion coefficients of the synoptic patterns identified from S*1a and S*1b modes; (a3) the regression between the SMB and the expansion coefficients of the synoptic patterns identified from S1, S2, S1* and S2* modes. r is the correlation coefficient between the original SMB from MAR and the SMB estimated from the linear regression. (b1), (b2) and (b3) show the standardized time series of the annual SMB anomaly from MAR (spatially averaged over the GrIS, orange bar) and the estimated SMB (black bar) from the linear regression described in (a1), (a2) and (a3). The significant r-value with 99% confidence is ±0.44.

References

Chen, L., Fettweis, X., Knudsen, E. M. and Johannessen, O. M. (2015), Impact of cyclonic and anticyclonic activity on Greenland ice sheet surface mass balance variation during 1980–2013. Int. J. Climatol.. doi:10.1002/joc.4565

Bergen Air Quality under Present and Future Climate Scenarios

Tobias Wolf, Igor Esau, Joachim Reuder[1]

[1] Geophysical Institute, University of Bergen

Here we will give an overview over our detailed study of the occurrence of high pollution events in the Bergen valley. The city of Bergen is located in a narrow valley at the west-coast of Norway. The sheltering effect of the surrounding mountains together with the high latitude at 60° N leads to the frequent occurrence of wintertime temperature inversions in the urban atmospheric boundary layer. This caused repeated occurrences of high and very high pollution levels from traffic-emitted nitrogen dioxide (NO_2), defined as measurements with hourly mean NO_2 concentrations of more than 150 and 200 $\mu g/m^3$, respectively, especially in direct proximity to major road junctions. Over the years, the occurrence of winter-days with such high pollution events has varied considerably. For studying the high pollution events, we used a combination of three studies on

- the statistics of the observed temperature inversions in the Bergen valley
- the large-scale circulation above the valley during high pollution events
- the circulation within the narrow valley during representative conditions based on high resolution Large Eddy Simulations (LES).

Main findings

Localization of the climate assessment, scenarios and projections is one of the most important problems of the science-based climate change adaptation.

This study describes the local climate of the Bergen. It introduces a simple meteorological index to describe the air quality climatology. The years of bad air quality return in about 10-15 years cycle, which is linked to the variability of the large-scale atmospheric circulation over the North Atlantic.

The local air quality scenarios determined by the large-scale atmospheric circulation were studied using the turbulence-resolving model PALM.

The observational study [*Wolf et al.*, 2014] revealed the direct coupling between the high pollution events and the temperature inversions. It however also showed that temperature inversions in the Bergen valley are a more common phenomenon than previously assumed. The inversion height usually reaches up to around 250 m above the valley floor – that is at sea-level – and temperature inversions are connected to a very consistent circulation both inside and above the valley (Fig. 1). Inside the valley low-level temperature inversions almost exclusively occur under down-valley winds (the valley opens towards a large sea-inlet, Bergen fjord, towards the northwest) and the wind-distribution above the valley has a heavy tail towards South-Easterly winds during temperature inversions and thus also during high pollution events, as suggested by the ERA-Interim re-analysis.

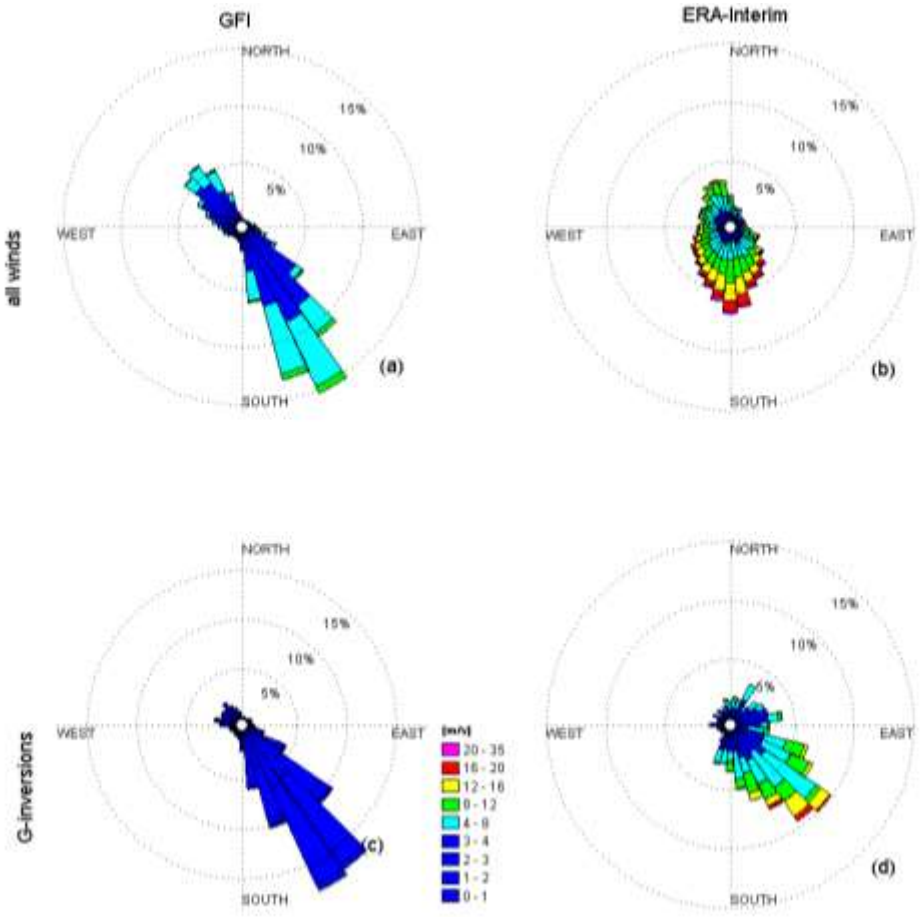

Figure 1. The measured wind distributions inside the Bergen valley (a,c) and the ECMWF ERA-Interim wind distributions over Bergen at model level 7, centered at 395 ± 6 m above ground level with ground level at 258 m above sea level (b,d) between March 2011 an February 2013. Subplots (a,b) show the general wind distributions during all weather conditions. Subplots (c,d) show the wind-distributions during ground-based temperature inversions (G-inversions). The common colour bar is shown in the lower right corner of (c). Percentage rings at 5, 10, and 15% indicate the fraction of the total valid data in each sector [*Wolf et al.*, 2014].

The consistent circulation above the Bergen valley during temperature inversions motivated the study on the large-scale circulation during high pollution events. We developed a simple atmospheric circulation proxy for days with favourable conditions for high pollution events based on the daily mean 1000 hPa or 10 m ERA-Interim wind-direction and speed, and the 2 m temperature deviation from its climatological seasonal mean cycle above Bergen [*Wolf and Esau*, 2014]. We tuned the proxy by simply taking suitable threshold for these quantities based on histograms for high pollution days (at least one hourly mean measurement of more than 150 $\mu g/m^3$) at a high traffic reference station and 'normal' conditions over the extended winter months (NDJF) since 2003, when the pollution measurement stations was installed. While not being usable as a case-by-case prediction tool, it reproduces the inter-monthly and seasonal variability of high air pollution days. The proxy has a high correlation of 0.89 and 0.93 with the occurrence of days with high pollution levels on a monthly and seasonal basis, respectively (Fig. 2). We also compared the occurrence of such events to the typically used large-scale circulation indices North Atlantic Oscillation (NAO), the Scandinavian index and the Euro-Atlantic blockings. None of the usual large-scale atmospheric circulation indices agreed as well with the occurrence of high pollution events as our simple proxy. In addition to observations from the high traffic reference stations, there are also measurements from an urban background station available. Maximum covariance analysis between the daily maximum pollution

concentration at the two measurement stations and the 500 hPa geopotential height anomaly from ERA-Interim suggested a negative NAO pattern to be the most dominant circulation pattern connected to high pollution levels. However, the correlation between the dominant modes of co-variability for the 500 hPa geopotential height anomaly and the pollution was low (R^2 of only 33 %) meaning that there is not one dominant atmospheric circulation pattern leading to days with high air pollution. Another conclusion of this study is that the usual Euro-Atlantic blockings are not the main steering parameter for the high pollution events, as we previously assumed. The necessary persistence of the atmospheric circulation to reach the high pollution events – it usually takes at least two days with persistent conditions for the high pollution levels to be reached – is rather connected to blockings upstream from Bergen, e.g. the Greenland blockings.

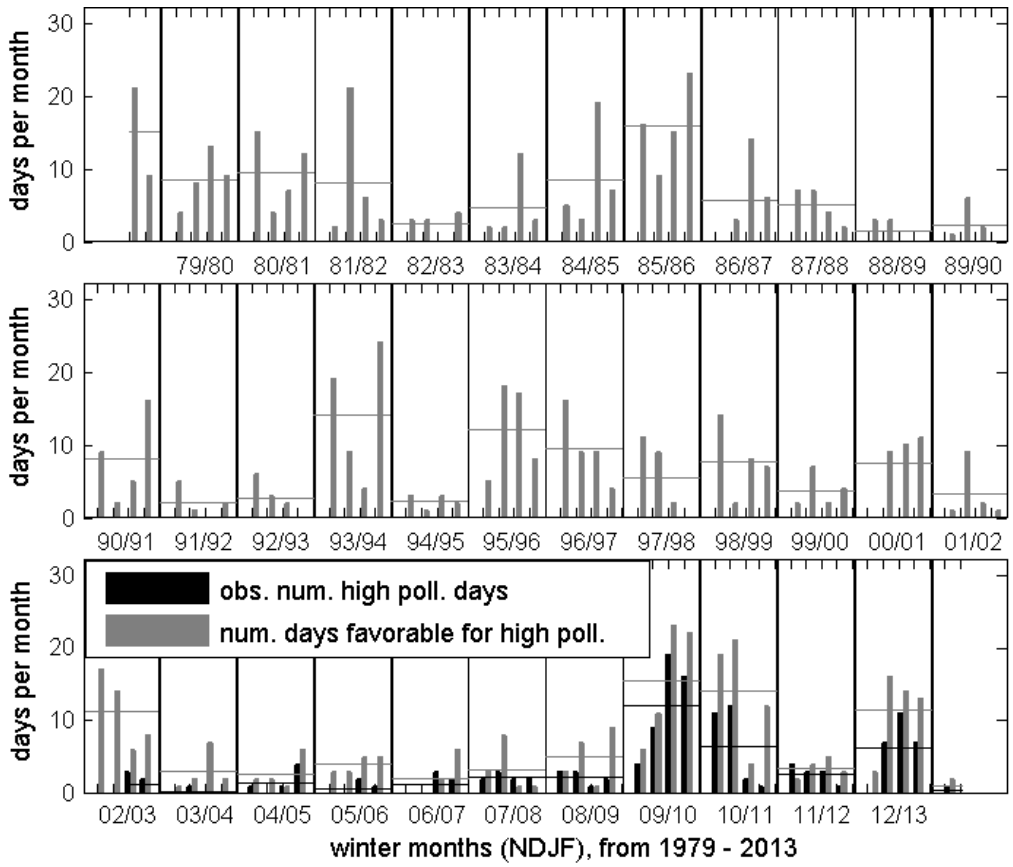

Figure 2: Monthly sum of observed days with high NO_2 air pollution and of days with favourable conditions for high pollution events for the extended winter seasons 1979 – 2013. The horizontal lines show the seasonal means of the monthly sums.

We also applied our proxy to two different climate models: The Norwegian Earth System Model (NorESM) and the Atmospheric General Circulation Model of the Japanese Meteorological Research Institute (MRI-AGCM). NorESM severely underestimated the total number of days with favourable conditions for high pollution events. On the other hand, the inter-annual variability of the occurrence of such days was represented better in NorESM. About the underestimation of the number of days with favourable conditions for high pollution events, we assume that the modification of the circulation by the Norwegian topography on a scale of the order of 50 – 100 km needs to be resolved in the model in order for our proxy to be applicable. Both models did not predict a significant change of the occurrence of high pollution days towards the end of the 21st century.

The underlying assumption for the development of such a large-scale circulation index was the strong steering of the high pollution cases within the valley by the local topographic features. In order to understand the potential connection between the large-scale circulation and the circulation within the valley we tried to simulate the typical circulation during high pollution events. For this we used the Parallelized Large Eddy Simulation Model (PALM) for idealized simulations with a prescribed geostrophic wind profile on a periodic grid, a prescribed surface sensible heat flux of –0.025 Km/s over land, prescribed surface temperatures over water and realistic topography (Fig. 3). The simulation domain included the inner Bergen valley and parts of the Bergen fjord. These simulations revealed the importance of the interplay between the local topography, the warm fjord and the cold land during high pollution cases for the dispersion of the air pollutants. With decreasing height, the prevailing south-easterly geostrophic winds are rotated to North-Easterly winds that then are channelled inside the valley to an up-valley flow. Simultaneously, the visible flow convergence over the fjord caused by the relatively warm water surface causes an up-valley flow above the valley floor. A simulation with zero surface sensible heat flux over the entire domain on the other hand showed an up-valley flow through the depth of the valley. This result has important implications for the dispersion of pollutants from the Bergen harbour, where ships are a major emission source for both NO_2 and particulate matter. Through sensitivity studies we found that the wind-direction and -speed in the middle of the valley was highly dependent on the balance between cooling over the land, the surface temperature over the Bergen fjord and the strength of the geostrophic wind.

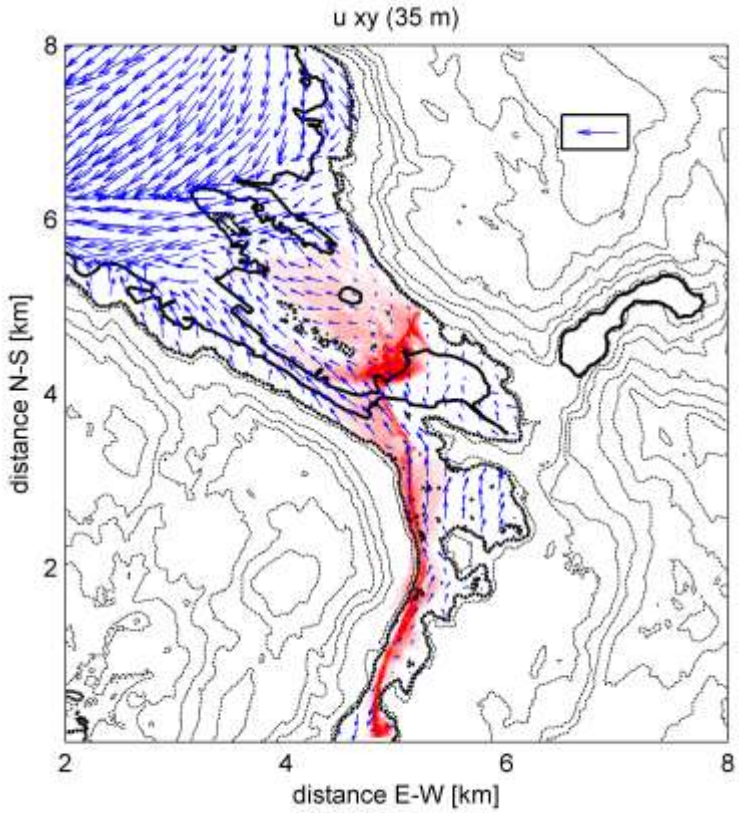

Figure 3: PALM simulation of the circulation in the Bergen valley connected to the typical south-easterly winds above the valley. The red shading shows the relative concentration of a passive tracer emitted from E39 (dark read means high concentrations), the wind-vectors show the wind-field close to the surface (35 m above sea level, the topographic contour is indicated with the thick dashed line). The wind-vector in the upper right corner indicates a wind of 3 m/s. The total domain size for this simulation was 1.024 x 1.024 km; only the inner, most relevant part of the domain is shown.

References

Wolf, T., and I. Esau (2014), A proxy for air quality hazards under present and future climate conditions in Bergen, Norway, *Urban Clim.*, *10*, 801–814, doi:10.1016/j.uclim.2014.10.006.

Wolf, T., I. Esau, and J. Reuder (2014), Analysis of the vertical temperature structure in the Bergen valley, Norway, and its connection to pollution episodes, *J. Geophys. Res. Atmos.*, *119*(18), 10,645–10,662, doi:10.1002/2014JD022085.

15-year record of normalized difference vegetation index (NDVI) reveals significant forest decline in NW Siberia

Victoria Miles and Igor Esau

Vegetation productivity trends are produced for NW Siberia for the period 2000–2014 and examined in the context of productivity response along climatic and forest composition gradient. The presence of evergreen and deciduous functional types across the boreal forest has not been previously assessed in relation to the observed increase or decline of productivity. The vegetation trends in this region have been previously assessed only as a part of general Eurasian trends in different pan-arctic studies. The current study updates and details the results of the previous NDVI max study for different parts of Arctic and focuses on observation of vegetation productivity specifically in NW Siberia and at relatively high resolution.

Main findings

Vegetation productivity trends (NDVImax index) are produced for North Western Siberia for the period 2000–2014.

The mapping reveals general greening (increasing productivity) in the northern biomes (tundra and tundra-forest). The map also shows widespread browning associated with evergreen and deciduous boreal forests.

In this study we focus on the regional and latitudinal distribution of NDVI max and its changes for the last 15 years in forest and tundra biomes in NW Siberia. We examined changes in vegetation productivity in NW Siberia using the variability in annual maximum NDVI. The study involves comparative analysis in four bioclimatic zones in the region: tundra, forest-tundra and northern open woodlands, boreal zone with northern and middle subzones (Fig. 1a,b). We collected information about the vegetation of the area based on distribution and variability of the NDVI index. The NDVI max in NW Siberia generally decreases from the southwest to the northeast of the territory (Fig.1a).

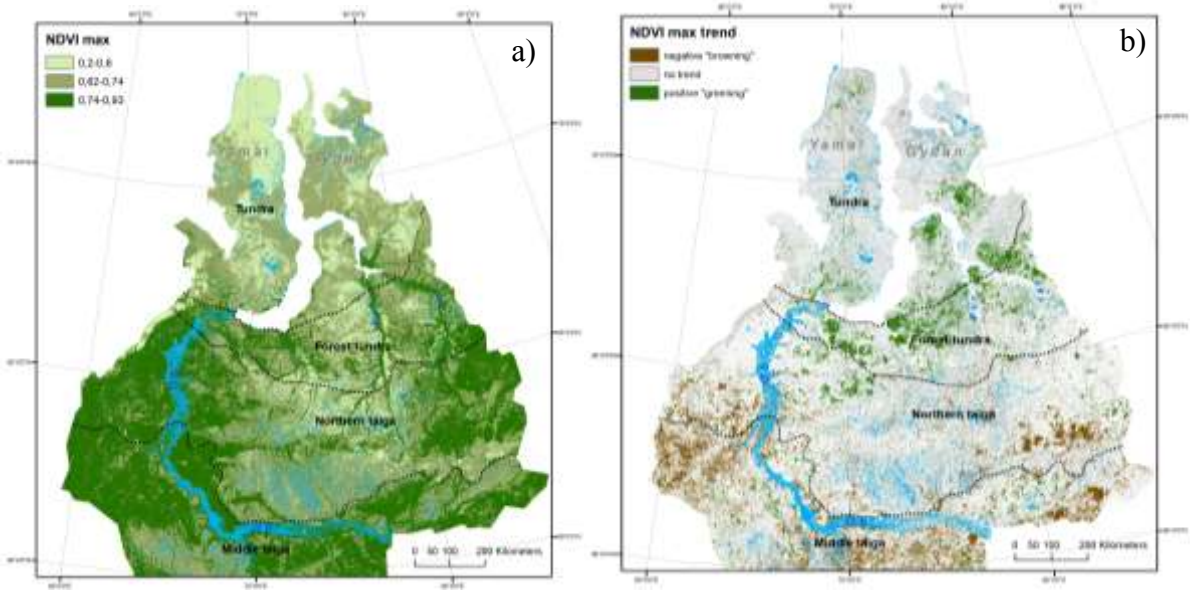

Figure 1. The 15-year mean NDVImax (a) and NDVImax trend 2000-2014 ($p<0.05$) (b).

The tundra has the lowest NDVI max values. The central, swamped part of the region is characterized by the much lower NDVImax, while the largest NDVImax is found for the most productive vegetation along the Ob River and between the Ob River and Ural mountains. Typically, the NDVImax is significantly higher on river terraces with better drained and therefore warmer soils. In the tundra, negative trends NDVImax pattern is highly fragmented and only small percent of all negative changes are in these two zones, which are in the northern part of the Gydan peninsula and eastern part of Yamal peninsulaThe distribution of 15-year trends calculated in our study is shown in Fig. 1b. Almost 90% of NDVI max changes in tundra and forest-tundra are positive. 60% of all positive changes in the entire NW Siberia are in these two zones (Fig. 2). The largest areas of greening are seen in the south parts of Gydan, Yamal and Tazovskiy peninsula and along Taz and Pur rivers. In general, all greening lies between 65° and 70°N latitude. In the taiga, the negative trends of NDVI max are prevalent and account more than 90% of all significant changes with a high concentration in southwest, south and southeast part of the study region.

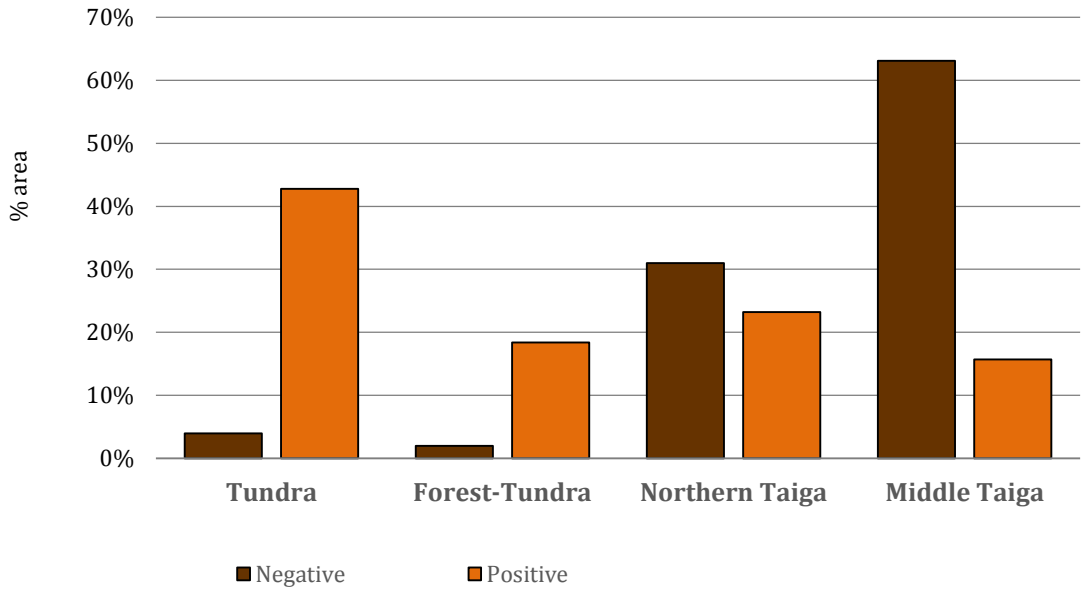

Figure 2. Proportion of statistically significantly trends between bioclimatic zones.

Light evergreen *Pinus sylvestris* and deciduous needleleaf *Larix sibirica* are dominant tree species in the Siberian forests in the study region and in Siberia in general; the biggest part of the study region is non-forested. In northern taiga forest covers 51% and in middle taiga 48%, which consist of 16% and 16.5% of the entire forested area of NW Siberia. About all negative trend on the entire area mainly associated with forest and especially with evergreen and evergreen dominated mixed forest (Fig. 3).

Comparison of trends between different forest types reveals that in general the more productive and dense forest (such as dark or light evergreen and evergreen majority mixed forest) show declining productivity – 76% of all negative trends for forested areas. Deciduous needleleaf forest dominating by larch (*Larix*) shows a universal increase in productivity in every bioclimatic zone in NW Siberia and54 % of all positive trends for forest. Browning of forest

and no forest vegetation have meridional gradient and occurred more frequently in the warmer part of the species ranges.

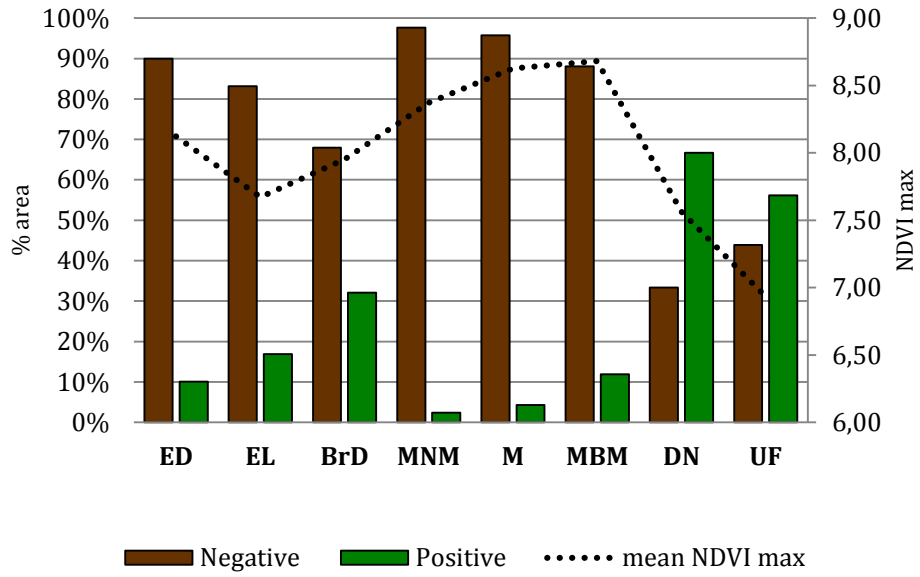

Figure 3. Trend stratification between different forest types. ED - Evergreen dark needleleaf forest consisting of spruce (*Picea)*, fir (*Abies*), and Siberian pine (*Pinus sibirica*); EL - Evergreen light needleleaf forest consisting of pine (*P. sylvestris*); BrD - Deciduous broadleaf forest consisting of birch (*Betula*), aspen (*Populus tremula*), oak (*Quercus*), linden (*Tilia*), ash (*Fraxinus)*, maple (*Acer*), and some other deciduous broadleaf tree species; DN - Deciduous needleleaf forest consisting of larch (*Larix*); MNM- Mixed needleleaf majority forest consisting of the evergreen needleleaf tree species and the deciduous broadleaf tree species; M - Mixed forest - Proportions of the evergreen needleleaf and the deciduous broadleaf tree species are approximately equal; MBM - Mixed broadleaf majority forest consisting of the deciduous broadleaf species and the evergreen needleleaf species; UF - Unforested areas - area covered with no tree vegetation.

Climate change is a powerful factor influencing the forest ecosystems. Adaptive mechanisms of plants develop for hundreds of millions of years, the speed of changes in average temperature conditions were much lower than at present. Beck & Goetz (2011) reported increasing tundra trends of vegetation productivity and decreasing productivity in boreal forest zone. The decrease in boreal forest productivity is most prominent in areas of denser tree cover. The positive trends in tundra are correlated with temperature; however, explaining the negative trend in the taiga zone remains inconclusive. The impact of higher autumn and winter temperatures may adversely affect the formation of the state of winter dormancy, growth and development of woody plants. Warming temperature were observed in winter and autumn in northern part of West Siberia. The response of tree growth to a change in temperature may differ. Elevated temperatures enhanced growth in deciduous species more than in evergreen trees [Way and Oren, 2010]. Siberian pine mortality observed in European Russia, Siberia, and the Russian Far East [Kharuk, 2009] coincided with areas of observed drought increase. Dark needle conifers may be replaced by drought-resistant *Pinus silvestris* and *Larix sibirica*. Siberian larch prefers light and is tolerant of both heat and frost.

The increase of air temperature and amount of precipitation cause the flat poorly drained surface of NWS plain process of bog development to become more active [Moskalenko, 2013]. As a result, the wood plant community replaced by bog plant communities. Comparison of biomass in wood communities and bog communities show that by bog formation all

aboveground biomass decreases on 26% and biomass of graminoid and mosses increase [Moskalenko, 2013]. Contrasting processes are occurring in the southern and northern parts of the Western Siberian Plain. In the south, bogs are expanding in the taiga zone and there is progressive swamping which leads to forest death. As a result, in this part of Western Siberia bogs act as a kind of 'global cooler' due to carbon sequestration in their peat layers. However, the situation in the northern part (affected by permafrost) is completely different. The bogs there are reducing their area and the forest-tundra area is being subjected to thermokarst activity and colonization of bogs by trees (Kripotkin). Analyses of climatic and vegetation productivity relationships of black spruce (*Picea mariana*) in North America indicate that forests has been decline via the enhanced moisture stress related with the retreat of Arctic sea [Girardin,et al., 2013].

In NW Siberia, the decline in productivity may be connected with different processes. NDVI pattern on the Yamal are only weakly correlated with the temperature and are most strongly related to factors determine environmental conditions designate vegetation growth potential [Walker, 2009]. The presence of browning and greening trends for the same forest type growing in same zone is likely due to variety in combination of these factors. Even within a small area – for example southeast part – characterized by the uniform physical and geographical conditions in different parts of it, we find the opposite changes.

References

Beck, P. & Goetz, S., 2011. Satellite observations of high northern latitude vegetation productivity changes between 1982 and 2008: ecological variability and regional differences. Environmental Research Letters, 6, p. 045501.

Kharuk, V.I. et al, 2013. Siberian pine decline and mortality in southern Siberian mountains. Forest Ecology and Management Volume 310, 15 December 2013, Pages 312–320

Moskalenko, N., 2013. Impact of climate warming on vegetation cover and. Natural Science, 5(1A), pp. 144-148.

Rapid changes in advance–retreat (co)variability of Sermilik fjord glaciers, southeast Greenland

Victoria V. Miles, Martin W. Miles [1,2] and Ola M. Johannessen

[2] Uni Research/Bjerknes Centre for Climate Research, Bergen, Norway
[3] Institute of Arctic and Alpine Research, University of Colorado, Boulder, USA

Numerous studies have indicated that increased discharge rates of marine-terminating outlet glaciers play a significant role in mass loss from Greenland; the most comprehensive estimates are that retreat and acceleration of outlet glaciers – notably in southeastern Greenland – account for 50% of Greenland's net mass loss since 2000 (van den Broeke et al., 2009). Therefore, understanding the variability and controls on outlet glacier dynamics is critical to improving predictions of ice-sheet variability and sea-level change.

Main findings

Numerous studies have indicated that increased discharge rates of marine-terminating outlet glaciers play a significant role in mass loss from Greenland.

This study shows that the seasonal amplitude of advance–retreat is important for the amount of calving. In the 1980s, calving amounts were large despite no overall retreat. Peak calving activity in mid 1980s and early 2000s.

Marine-terminating Greenland Ice Sheet outlet glaciers have recently been found to vary more rapidly than previously believed. Among the most dynamic are the outlet glaciers in southeast Greenland. Three major outlet glaciers – Helheim, Fenris and Midgård – terminate in the upper part of Sermilik fjord, the largest fjord system in southeast Greenland (Fig.1). Their close proximity, only 7–15 km apart from each other, suggests that the glaciers are under the same atmospheric and oceanic regime, and thereby may have a common response to variability in external forcing. The range of variability and the degree of co-variability between them is poorly known except for the past decade, as there are few studies of the long-term variability of glacier calving at high temporal resolution.

Figure 1. Sermilik fjord glaciers: Helheim, Fenris and Midgård.

We exploited the satellite archives to develop a new long-term high-resolution record of calving front position for Helheim Glacier, 1980–2011, as detailed in Miles et al. (2016). Analysis of this record has revealed new aspects that nuance the previous understanding of its variability. The front position has undergone abrupt changes in variability and mean, with major change points in 1991, 2001, 2005 and 2006, and secondary change points within the 1980s denoting sub-decadal changes (Fig. 2).

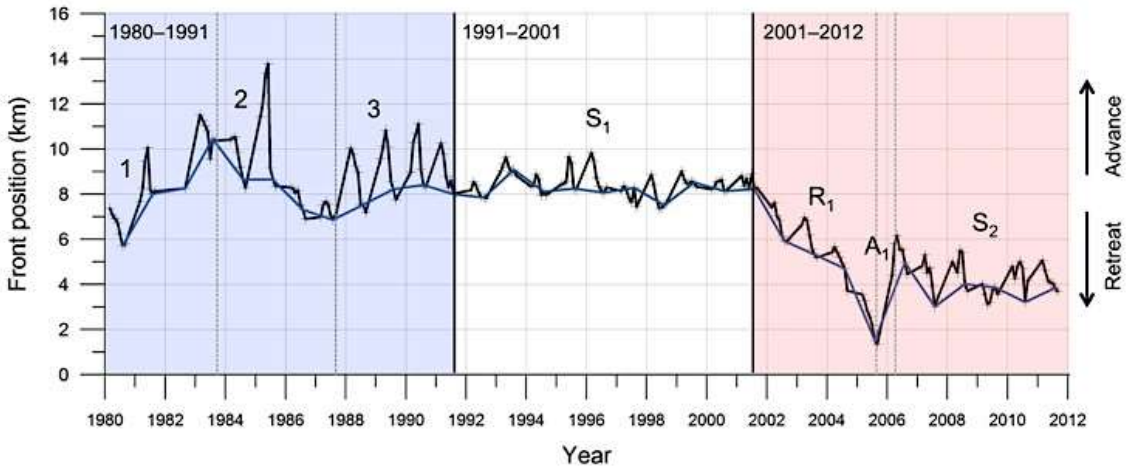

Figure 2. Helheim Glacier front position. Blue line: Annual values, Black line: Subannual values. Shading indicates three decadal periods of different variability, the dashed gray lines delimit sub-periods. Stable periods/sub-periods with stationary means are labeled S1 and S2. Large-amplitude variations: (1) multiyear advance, 1980–83; (2) "surge-like" advance 1984–85 and retreat 1985–86; (3) enhanced seasonal advance–retreat oscillation, 1987–91; (4) multiyear retreat, 2001–05; and (5) re-advance, 2005–06. From Miles et al. (2016).

Two periods of stability – 1991–2001 and 2006 onward – are characterized by stationary mean and low variability (< 2 km yr-1), although the mean front position $\bar{x}$ from 2006–onward is 5.1 km farther back than $\bar{x}$ from 1991–2001 (Fig. 2). These positions may represent "preferred" positions for the glacier, due to grounding and bed topography. There was volatile front-position behavior in the 1980s, with several large-amplitude advance–retreat episodes on subannual to interannual time scales, including a 6-km "surge-like" advance in 1984/85 – behavior that has not been recorded in previous studies of Helheim Glacier (Fig. 3).

There is some correspondence between the front position behavior and ice mélange associated with fluctuations of temperature and ocean conditions (Fig. 4); however the magnitude of at least the 1984/85 advance appear greater and changes in variability more abrupt than would be expected as a glacio-climatic response; thus glacio-dynamics are important. Dynamic advance–retreat behavior during the cold 1980s with reduced air and ocean temperatures resulted in calving amounts were greater in the 1980s than in the warm 2000s. This confounds the interpretation of increased ice discharge as a response to the climate warming.

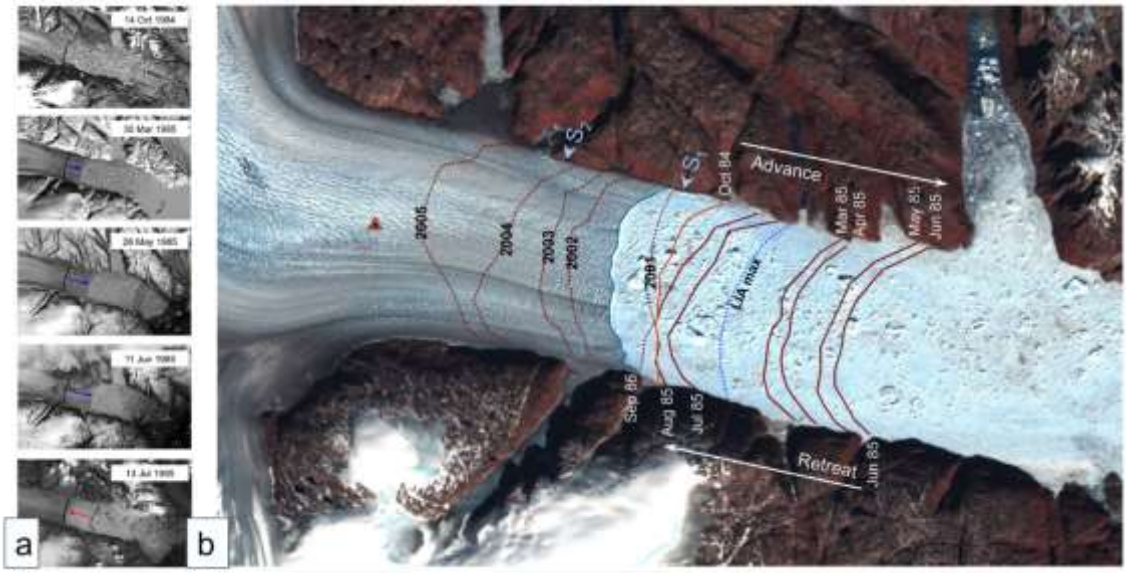

Figure 3. (a) Landsat image sequence of rapid advance and retreat of Helheim Glacier, 1984–85. (b). Comparison of the rapid advance–retreat 1984/85 and the multi-year retreat in the early 2000s. The solid red lines show the advance in 1984–85 and retreat in 1985–86. The dotted red lines - the yearly position during the retreat in the early 2000s. The blue dotted line is Little Ice Age (LIA) maximum (Khan and others, 2014). The orange arrows indicate the mean position during the stable periods 1991–2001 (S1) and 2006 onwards (S2), as in Fig 2. The red triangle is the 0-point for the front-position measurements plotted in Fig. 2. From Miles et al. (2016).

Figure 4. Helheim Glacier calving front and comparison with climate data, 1980–2011: (a) Calving-front position (black) and annual surface air temperature record (red) from the nearest station, Tasiilaq, (b) Shelf index, an indicator of the relative amount of polar water and sea ice on the southeast Greenland shelf (from Andresen et al., 2012), (c) winter ice mélange conditions (light blue = rigid, grey = mixed, and red = open), and (d) Indicator of calving activity; horizontal bars are the mean annual calving losses in each decadal period. 1982 – no observations. From Miles et al. (2016).

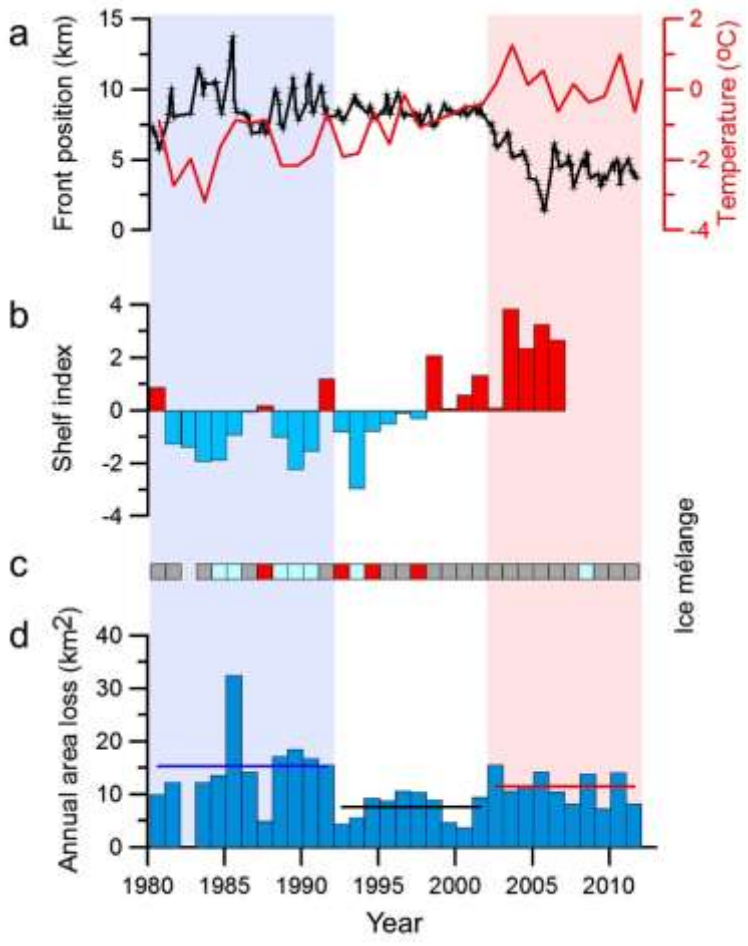

Comparison of 30^{+}-year time series for Helheim, Fenris and Midgård glaciers identifies decadal sub-periods when the glaciers exhibit different advance–retreat (Fig. 5 and Table 1). Midgård glacier behaves very differently than Helheim and Fenris glaciers in the past decade. Midgård glacier shows unabated retreat during the 30-year period.

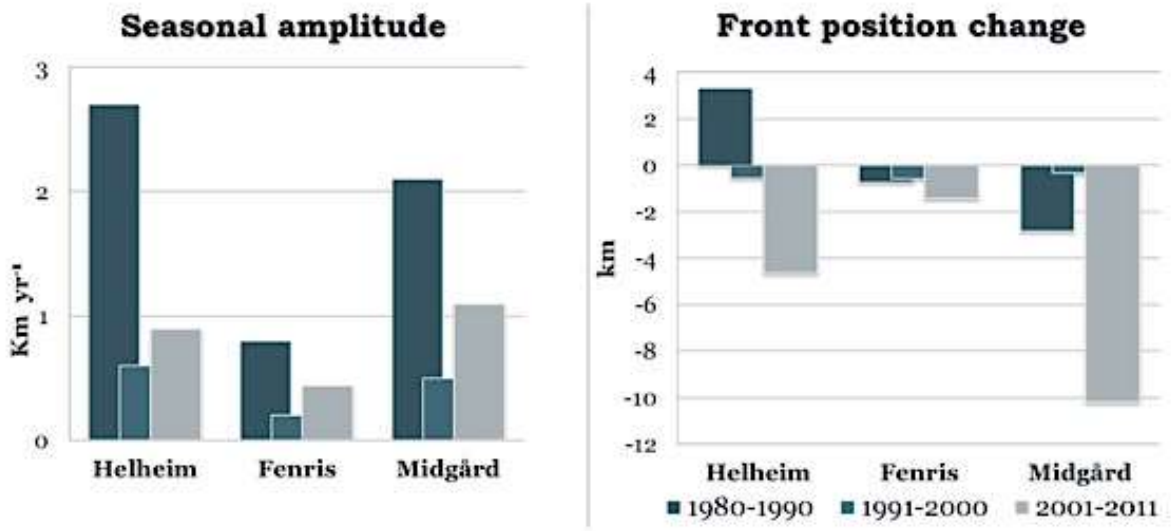

Figure 5. Glacier-front (co)variability over three decades. (a) Large seasonal cycle in 1980s for all glaciers. (b) No overall advance or retreat in the 1980s, but large retreat in the 2000s.

Table 1. Correspondence of glacier-front variability during different periods.

Correlation (*r*) of front position	**1980–90**	**1990–2000**	**2000–11**	**1980–2011**
Helheim–Fenris	0.7	0.7	0.6	0.7
Fenris–Midgård	0.6	0.2	0.03	0.3
Helheim–Midgård	0.7	0.7	0.1	0.4

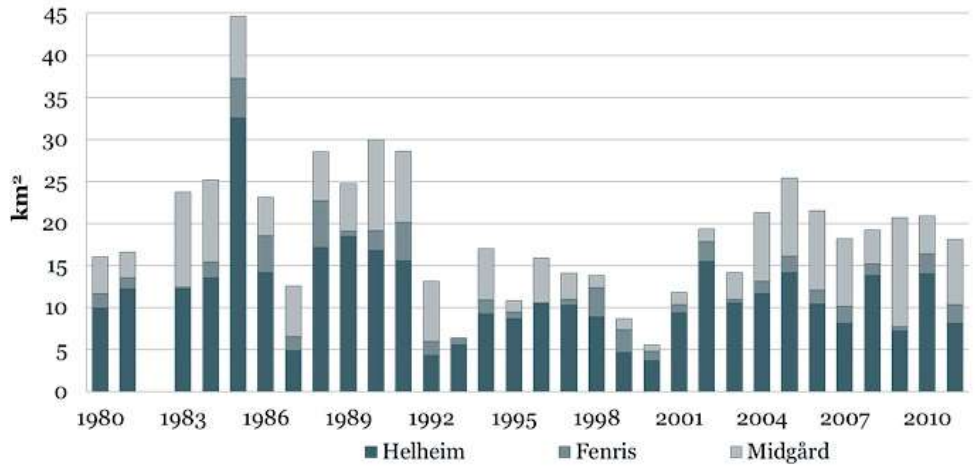

Figure 6. Sermilik fjord glacier calving activity over three decades.

We find that the seasonal amplitude of advance–retreat is important for the amount of calving. (Fig. 6) In the 1980s, calving amounts were large despite no overall retreat. Peak calving activity in mid 1980s and early 2000s, in general agreement with a calving proxy record (Andresen et al., 2012).

These findings underscore the complexity of marine-terminating Greenland outlet glacier variability (Post et al., 2012) and point to the need for further exploration of the satellite and aerial photo archives (e.g., Bjørk et al., 2011; Kjær et al., 2012) to develop and analyze similar long-term, high-temporal-resolution records of other major Greenland outlet glaciers, in order to constrain and understand their natural variability and response to climate forcing.

References

Andresen, C.S. et al. (2012), Rapid response of Helheim Glacier in Greenland to climate variability over the past century. *Nature Geosci*., 5, 37–41 (doi: 10.1038/NGEO1349)

Bjørk, A.A. et al. (2012), An aerial view of 80 years of climate-related glacier fluctuations in southeast Greenland. *Nature Geosci*., 5, 427–432 (doi: 10.1038/NGEO1481)

Howat, I.M., Joughin, I., Tulaczyk, S. and Gogineni, S. (2005), Rapid retreat and acceleration of Helheim Glacier, east Greenland. *Geophys. Res. Lett*., 33, L22502, doi: 10.1029/2005GL024737

Joughin, I. et al. (2008), Ice-front variation and tidewater behavior on Helheim and Kangerdlugssuaq glaciers, Greenland. *J. Geophys. Res*., 113, F01004 (doi: 10.1029/ 2007JF000837)

Kjær, K.H. et al. (2012) Aerial photographs reveal late-20th-century dynamic ice loss in Northwestern Greenland. *Science*, 337, 569–573 (doi: 10.1126/science.1220614)

Luckman, A., Murray, T., de Lange, R. and Hanna, E. (2006), Rapid and synchronous ice-dynamic changes in East Greenland. *Geophys. Res. Lett*., 33, L03503 (doi: 10.1029/2005GL025428)

Miles, V.V., Miles, M.W. and Johannessen, O.M. (2016). Satellite archives reveal abrupt changes in behavior of Helheim Glacier, southeast Greenland. *J. Glaciol.* 62, in press.

Moon, T., Joughin, I. and Smith, B. (2015), Seasonal to multi-year variability of glacier surface velocity, terminus position, and sea ice/ice mélange in northwest Greenland. *J. Geophys. Res.*, 120, 818–833 (doi: 10.1002/2015JF003494)

Post, A., O'Neel, S., Motyka, R.J. and Streveler, G. (2012), A complex relationship between calving glaciers and climate. *EOS Trans. Amer. Geophys. Union*, 92, 305–312 (doi: 10.1029/2011EO370001)

van den Broeke, M. et al. (2009). Partitioning recent Greenland mass loss. *Science*, 326, 984–986 (doi: 10.1126/science.1178176)

Mapping the surface air temperature over complex terrain by kriging with external drift from a large-eddy simulation model.

Igor Esau and Mikhail Varentsov[1]

[1] Moscow State University, Moscow

Information about surface air temperature is widely used for many practical purposes. The existing observational networks of meteorological stations are often too sparse to provide this information at required spatial resolution. Therefore, temperature mapping relies on statistical and model-based interpolation algorithms. We explored a set of kriging algorithms with variorgam analysis, namely: ordinary kriging (OK); universal kriging (OK_LES) with external drift from high-resolution large-eddy simulations. The geostatistical kriging algorithms are known as robust and efficient methods, because they account for spatial variability of data through the variogram analysis. However, as any statistical methods, the OK method cannot predict extremes between nodes of the observational network. Such extremes are common for the temperature fields in mountainous coastal areas where the temperature contrasts could be large both on the slopes and at seashore. Moreover, the extremes may have large impact, and hence, are of the strongest interest for users of the temperature maps.

Main findings

Local climate assessment requires spatial interpolation of the meteorological observations from a sparse network of stations.

This study investigates a set of geostatistical kriging methods, which include an additional information about the temperature field from a turbulence-resolving simulations. We demonstrate that such simulations has significant added value over complex surfaces as they introduce information about the temperature variability beyond the stations' radius of representation.

To reduce these drawbacks, we propose to utilize the fully three-dimensional Parallelized Atmospheric Large-eddy simulation Model (PALM) runs as the external drift and as the input into the variogram analysis in UK methods. The proposed method is demonstrated in a case of high-resolution (30 m) temperature mapping for Bergen, Norway.

We used the temperature data from seven AWSs listed in Table 1. These stations represent different microclimatic conditions. Nordnes is located on a peninsula surrounded by water. Florida and Haukeland are located in the low, urban part of the valley. Strandafjellet and Ulriksbakken are found on steep northern and western hill slopes correspondingly, whereas Løvstakken and Ulriken are the summit AWSs at the altitudes 472 m and 605 m above sea level.

The meteorological temperature profiler MTP-5HE scans the atmospheric temperature in the range of heights between 45 m and 1045 m above sea level in the direction of southern Bergen valley. The description of this instrument and its data set as well as the intercomparisons of the AWS and MTP-5HE data could be found in Esau et al. (2013) and Wolf et al. (2014). In this study, we use the hourly averaged AWS and MTP data.

Table 1. *Location and elevation of automatic weather stations in Bergen region, used in this research.*

№	Station name	Lon., °N	Lat., °E	Sensor elevation a.s.l, m	Sensor elevation a.g.l., m	Surface elevation a.g.l. from ASTER, m
1	Ulriken	60.377	5.379	605	4	533
2	Ulriksbakken	60.379	5.373	408	2.5	332
3	Haukeland	60.380	5.362	64	10	47
4	Florida	60.384	5.332	48	30	10
5	Løvstakken	60.360	5.321	472	2.5	426
6	Strandafjellet	60.372	5.323	303	2.5	242
7	Nordnes	60.4	5.304	48	30	10

For this study, we selected May 27 of 2011 when the lower atmosphere was well-mixed and no precipitation was recorded. During this period, north-west cardinal wind direction (taken from the observation at Ulriken) were observed as listed in Table 2. SAT at Nordnes AWS is strongly affected by the much colder SST and is by 3-4 °C lower than SAT at other stations. SAT at AWSs is usually higher that the temperature from MTP-5HE at the same height as the AWS measures the temperature within the overheated surface layer, whereas the profiler provides the temperature of the free atmosphere. The difference depends on the solar angle and the local wind speed and direction. These deviations are hard to account with ad hoc external drift models for the temperature mapping, and therefore, they are of primary interest for the proposed kriging methods with the external drift from the LES model.

Table 2. *Overview of cases, selected for detailed analysis. Case time is related to the end of one hour averaging period.*

Case name	Date and time	Wind at Ulriken		Mean temperature gradient (-dt/dz) over Florida from MTP-5HE, °C/100 m
		Dir, °	Spd, m/s	
NW	27.05.2011 12:00	304	2.9	0.91

Reconstruction of the temperature anomaly field, ΔT, revealed significant problem: the available number of observation points is insufficient for solving the problem of experimental variogram fitting. Firstly, seven meteorological stations around Bergen valley are located relatively far from each other, so there are no data at the beginning of experimental variogram. In addition, a significant part of the stations (3 of 7) is located in relatively similar conditions – at the mountain summits, so in some cases they could have similar values of variables. Therefore, experimental variogam, calculated using station measurements, could looks very chaotic in some cases (Figure 1) because of lack of the data. In attempt to solve this problem, we construct ΔT_{mat} using MATLAB®4 griddata method $griddata\ [z_s, x_s, x_p]$ where z_s are variable values at sampled points x_s and x_p coordinates of points where spatial prediction is needed. This method is applied only for interpolation triangle (see Fig. 1). This gridded field

provides much smoother variogram, which could be easily approximated by theoretical variogram model and used in kriging procedure:

$$\Delta T_{OK}(x_R) = OK[\Delta T_{i=1\dots n}, x_{i=1\dots n}, x_R, var\ (\Delta T_{mat}(x_R), x_R)] \qquad (1)$$

where $OK[z_s, x_s, x_p, v]$ is designation for ordinary kriging procedure which takes as arguments variable values z_s at sampled points with coordinates x_s, varioriogramm model γ and coordinates of points x_p where spatial prediction is needed, and $var\ (z_s, x_s)$ is designation of the procedure, which builds empirical variogram and fits theoretical variogram model to it.

Now it is possible to obtain air temperature field according our general approach:

$$T_{1\,OK}(x_R) = T_0(x_R) + \Delta T_{OK}(x_R) \qquad (2)$$

As an alternative, it is possible to apply the same special prediction procedure directly for the temperature T instead of ΔT:

$$T_{mat}(x_R) = griddata\ [T_{i=1\dots n}; x_{i=1\dots n};\ x_R] \qquad (3)$$

$$T_{2\,OK}(x_R) = OK[T_{i=1\dots n}, x_{i=1\dots n}, x_R, var\ (T_{mat}(x_R), x_R)] \qquad (4)$$

Examples of $T_{1\,OK}$ and $T_{2\,OK}$ fields for NW case, in comparison with T_0 field are shown in Figure 1. It is evident that $T_{2\,OK}$ field looks spiller than $T_{1\,OK}$ field because it is build without taking into consideration influence of relief and stratification of the atmosphere – it is just an interpolation of the AWS observation data, while $T_{1\,OK}$ looks like T_0 field, fitted to AWS observations.

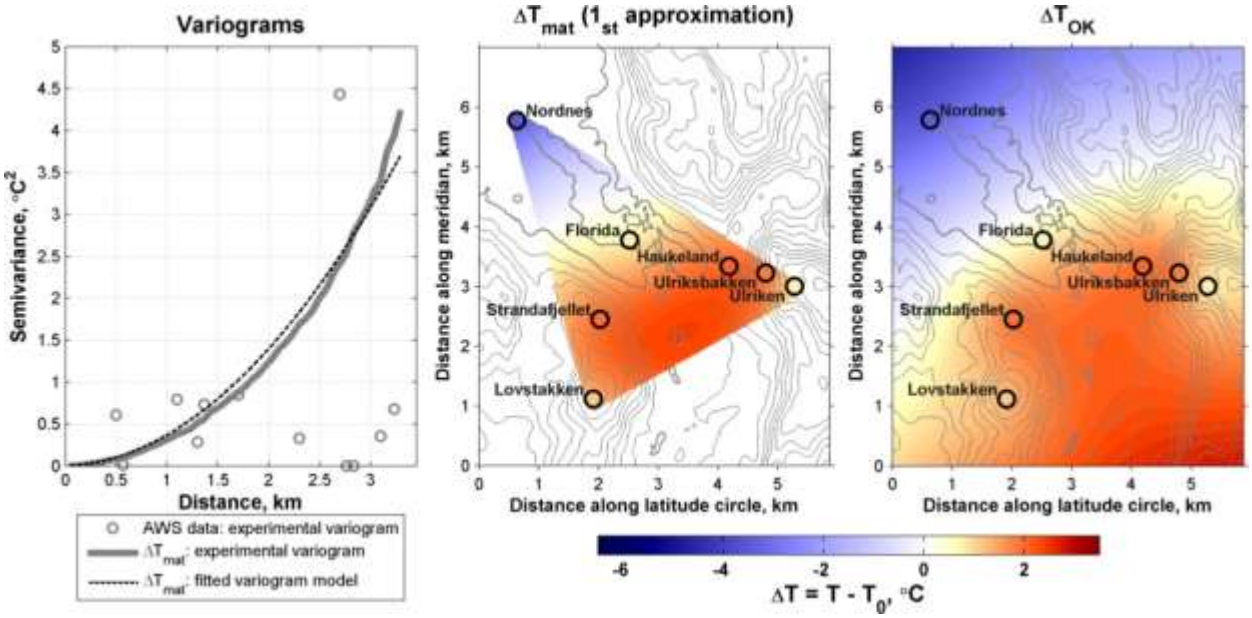

Figure 1. Comparison between experimental variograms for ΔT, based on the AWS scattered data and based on the first approximation field (right) for **NW** case, first approximation field (center) and field of ΔT_{OK} (right) for **NW** case.

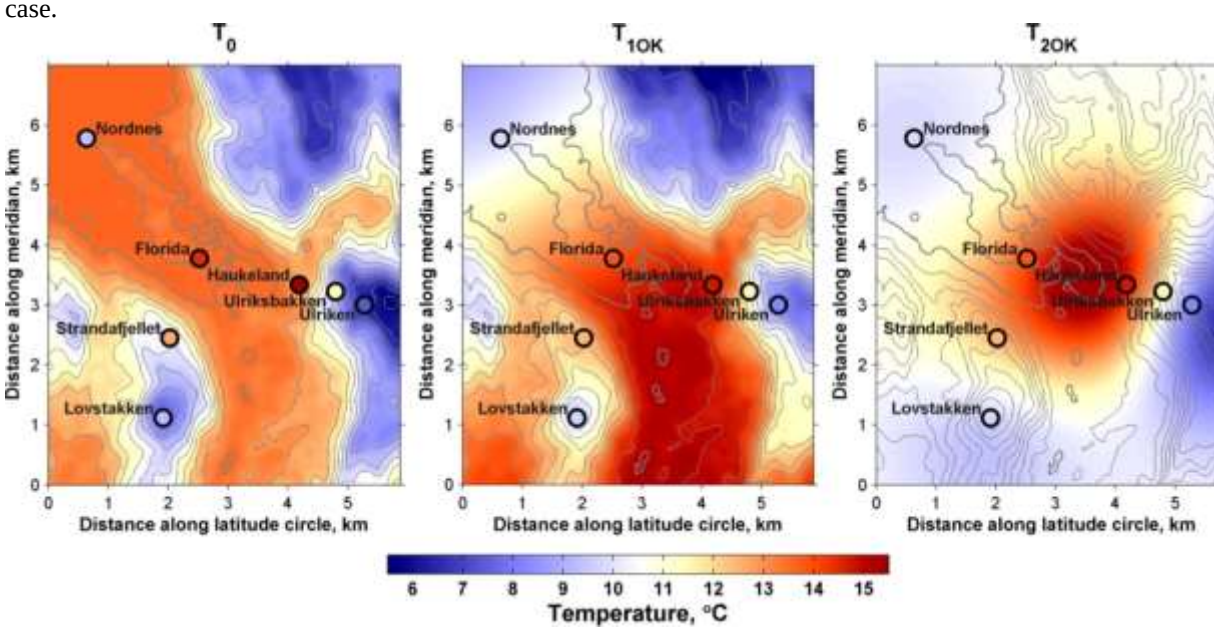

Figure 2. *Visualization of T_0 (left), $T_{1\,OK}$ (center) and $T_{2\,OK}$ (right) fields for NW case. Colored circles shows source values of AWS temperature observations.*

Experiments with LES-model, launched with initial conditions according temperature profiler and AWS observations for selected case, provided three-dimensional field of potential temperature, which could be easily recalculated to usual thermodynamic temperature $T_{LES}(x_{R3D})$. From this three-dimensional filed, two-dimensional field of the temperature at the first level over the surface $T_{LES}(x_R)$ could be obtained. This field can be used for calculating experimental variogram for air temperature, and which could be used as variogramm source for ΔT field.

LES model has been initiated by T_{mtp}, but the resulted temperature fields could be shifted by cooling or heating trend during the integration process, so we need to use T_{oLES} field, which is a model reflection of T_o. Such field could be easily calculated according modelled temperature profile over Florida point T_{mtp_LES}, cut from three-dimensional temperature field T_{LES}:

$$T_{0LES}(x_R) = T_{mtp\_LES}(z_{ASTER}(x_R) - z_{mtp}) \qquad (5)$$

Now we could obtain the field of variable ΔT_{LES}:

$$\Delta T_{LES}(x_R) = T_{LES}(x_R) - T_{0LES}(x_R) \qquad (6)$$

This field is used for calculation of a smooth experimental variogram easily-approximated by theoretical models and used in ordinary kriging procedure for spatial prediction of ΔT:

$$\Delta T_{OK\_LES}(x_R) = OK[\Delta T_{i=1\ldots n}, x_{i=1\ldots n}, x_R, var\,(\Delta T_{LES}(x_R), x_R)] \qquad (7)$$

The final temperature field becomes

$$T_{1\,OK\_LES}(x_R) = T_0(x_R) + \Delta T_{OK\_LES}(x_R) \quad (8)$$

Moreover, spatial prediction for the temperature field itself with variogram from LES model could be done as

$$T_{2\,OK\_LES}(x_R) = OK[T_{i=1\ldots n}, x_{i=1\ldots n}, x_R, var\,(T_{LES}(x_R), x_R)] \quad (9)$$

The main feature of external drift kriging is its possibility to fit the field of independent variable to the data in sampled locations. In our case, we could use the model variables (ΔT_{LES} or T_{LES}) as drift fields and fit them to observed data. Finally, we obtain for ΔT:

$$\Delta T_{KED}(x_R) = KED[\Delta T_{i=1\ldots n}, x_{i=1\ldots n}, x_R, \Delta T_{LES}(x_R), var\,(\Delta T_{LES}(x_R), x_R)] \quad (10)$$

where $KED\ [z_s, x_s, x_p, d, \gamma]$ is external drift kriging procedure, which takes same arguments as OK plus the drift field d, sampled at locations x_p.

Figure 3 illustrates the external drift kriging. One could observe that while ΔT_{LES} has detailed structure, this structure does not match the observation data, and kriging with external drift procedure shifts and scratches the drift field to fit it to the observations. Resulting field ΔT_{KED} differs strongly from fields $\Delta T_{OK\ LES}$ and ΔT_{OK} and is much more detailed. Influence of the cold sea is taken into account in it in way that is more realistic.

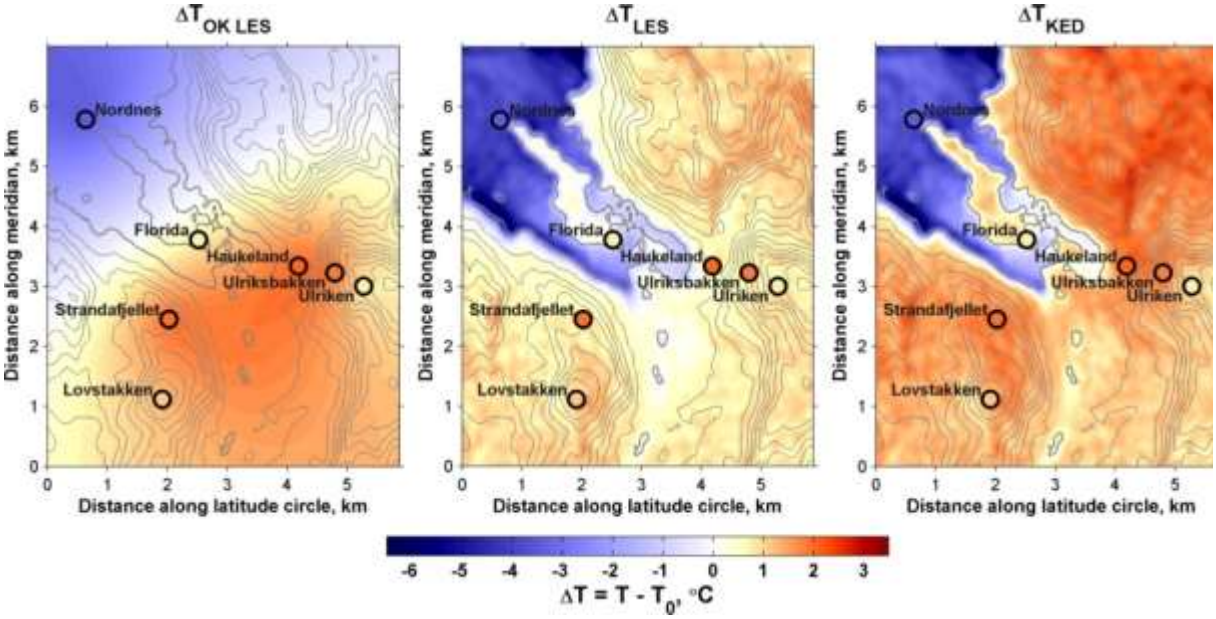

Figure 3. Comparison between $\Delta T_{OK\ LES}$, ΔT_{LES} and ΔT_{KED} fields for NW case.

References

Wolf, T., I. Esau, and J. Reuder, 2014: Analysis of the vertical temperature structure in the Bergen valley, Norway, and its connection to pollution episodes, J. Geophys. Res., 119, doi:10.1002/2014JD022085

Esau, I., T. Wolf, E. Miller, I. Repina, Y. Troitskaya, S. Zilitinkevich, 2013: Analysis of remote sensing monitoring of the lower atmosphere temperature profile in Bergen, Norway, *Russian Meteorology and Hydrology*, 10, 93-103

Acknowledgements

The group members were involved in 2015 in the following research projects.

Project No.	Funding agency	Title	Main Objectives
111100	SKD	BASIC: Boundary Layers in the Arctic Atmosphere, Seas and Ice Dynamics	To reconcile the observed climate features in the "new Arctic" with the identified and emerging physical/dynamical processes in the boundary layers (BLs) across the air-sea-ice interface.
111122-2	EC – H2020	GAIA-CLIM: Gap analysis for Integrated Atmospheric ECV Climate monitoring	To document the gaps and remedies, with advised prioritization, in how to use non-satellite measurements to characterize, calibrate and validate satellite measurements.
111005	EC – FP7	CoCoNet: Towards Coast to Coast NETworks of marine protected areas (from the shore to the high and deep sea), coupled with sea-based wind energy potential.	To provide a knowledge-base and tools for regional networks of MPAs, integrated management of activities together with assessment of wind energy potential in the Mediterranean and the Black Sea.
111091	NordForsk (Network)	CRAICC-PEEX:Cryosphere-Atmosphere Interactions in Changing Arctic Climate, and the Pan-Eurasian Experiment project.	To bring together researchers from Europe, Russia and China to coordinate future research activities in the Eurasian region.
111076	NRC (FRINAT)	Does the Arctic sea-ice loss have an impact on the winter weather patterns in Europe?	To create new knowledge of the linkage between cold spell in Europe and changes in the Arctic with a long-term perspective.
111017	GC Rieber Fondene	Bergen Air Quality under Present and Future Climate Scenarios	To develop methodology for the understanding of air pollution episodes in stably stratified urban boundary layers in complex terrain.
111114	SKD	MEchanisms of multi-DEcadal VAriability in the Climate system (MEDEVAC)	The primary goal of this project is to identify and investigate key mechanisms of multidecadal variability in the climate system by analyzing state-of-the-art climate model simulations and high-resolution paleoclimate reconstructions covering the last two millennia.
111104	SKD	Greenland Margins: Glacial Ice, Ocean and Atmospheric Dynamics (MARGINS)	MARGINS will improve understanding of changes in the Greenland margins and improved assessment of future perspectives.
111150	SKD	BjerknEs COMpEnsation and the sub-polar GYRE (BECOME-GYRE)	Investigate the links between Bjerknes Compensation and the strength of the sub-polar gyres in a range of CMIP5 models with an aim to developing a clear mechanism underlying the multi-decadal variability.